RWTH Aachen
JCNS-2 in Forschungszentrum Jülich

Voltage Control Of Crystalline Structure and Non-volatile Magnetoelectric Coupling Of LSMO/PMN-PT Heterostructure

---

Bingqing Wang

Thesis submitted
within the Material Science
Master thesis

Supervisor: Prof.Dr.Thomas Brückel/Prof.Dr.Joachim Mayer
Second Examiner: Dr. Emmanuel Kentzinger

May 19, 2022

©2021 – Bingqing Wang
All rights reserved.

Zusammenfassung

Die Manipulation magnetischer Eigenschaften durch elektrische Felder ist derzeit von großem Interesse für die Perspektive, Spintronik-Geräte mit niedrigem Energieverbrauch zu realisieren. Hier wird die Wirkung des elektrischen Felds auf die magnetische und kristalline Struktur des ferromagnetischen LSMO-Dünnfilms untersucht, der epitaktisch auf einem ferroelektrischen PMN-PT-Substrat aufgewachsen wird. Durch das Anlegen eines elektrischen Feldes an die Probe werden Kristallstruktur, Polarisation, Magnetisierung und Curie-Temperatur effektiv modifiziert. Der Mechanismus der Manipulation dieser Eigenschaften durch das elektrische Feld wird der Spannungsvermittlung und Ladungsvermittlung zugeschrieben, die durch die Polarisation verursacht werden. Basierend auf 71° und 109° ferroelastischer Domänenumschaltung des Substrats kann ein nichtflüchtiges Schalten des Magnetismus erreicht werden, der eng mit dem relativen Anteil der Polarisationsvektoren in der Ebene und den induzierten unterschiedlichen Dehnungszuständen in der Ebene nach dem Domänenwechsel zusammenhängt.

Abstract

The electric field manipulation of magnetic properties is currently of great interest for the opportunities provided for low-energy-consuming spintronics devices. Here, the effect of electric field on magnetic and crystalline structure of the ferromagnetic LSMO thin film, which is epitaxially grown on PMN-PT ferroelectric substrate, is investigated. With the application of electric field to the sample, the crystalline structure, polarization, magnetization and Curie temperature are effectively modified. The mechanism of the electric field manipulation of these properties is ascribed to the strain mediation and charge mediation caused by the polarization. Based on 71° and 109° ferroelastic domain switching of the substrate, non-volatile switching of magnetism can be achieved, which is closely related to the relative proportion of in-plane polarization vectors and induced distinct in-plane strain states after domain switching.

Contents

Chapter 1

Introduction

Altering the magnetic and electric phases in reversible and nonvolatile states by voltage control is the central challenge nowadays. Magnetoelectric heterostructures have aroused great interest in low-energy-consuming devices due to their coupling mechanisms. The ME effects reveal that the magnetization is controlled by electric field, or vice versa. The electric field manipulation of magnetism is a research focus since it can provide a low-consuming method to control the magnetization. It can be explained by Maxwell's equation that magnetic interaction and electric charge motion are intrinsically coupled.

The most used ME mode is related to two explanations: stain mediation [13] and charge coupling [7]. ME heterostructure consisting of ferromagnetic and ferroelectric components are widely used due to the strong physical properties coupling. In order to observe these mechanisms, different artificial heterostructure materials are developed such as $Fe/BaTiO_3$ [13], $La_{0.67}Sr_{0.33}MnO_3/BaTiO_3$ [33], $CoFe/BiFeO_3$ [30] and $La_{0.7}Sr_{0.3}$ $MnO_3/$ $[Pb(Mg_{1/3}Nb_{2/3})O_3]_{0.7}$-$[PbTiO_3]_{0.3}$[38]. In these heterostructures several research about the voltage induced non-volatile tuning of physical parameters can be achieved by using the non-linear lattice strain effects arising from the non-180° ferroelectric polarization reorientation.

In this thesis, we fabricated epitaxial LSMO thin film on (001) and (111)-oriented $[Pb(Mg_{1/3}Nb_{2/3})O_3]_{1-x}$-$[PbTiO_3]_x$(PMN-PT) ferroelectric single-crystal substrates. PMN-PT exhibits the excellent piezoelectric properties and ferroelectricity due to its perovskite structure. There are eight equal polarisation in $< 111 >$ direction and three switching domains $71^\circ, 109^\circ (ferroelastic)$ and 180°(ferroelectric) [16]. $La_{0.7}Sr_{0.3}MnO_3$ shows strong ferromagnetization via double exchange interaction of $Mn^{3+}$and Mn^{4+} [20].

Through manipulation of the electric field a unique ferroelastic switching(71° and 109°) pathway in PMN-PT was exploited to produce distinct lattice strain states by rotating the polarization vectors between out-of-plane and in-plane directions. In this way, stable non-volatile magnetization can be generated at room temperature. Meanwhile, the ME coupling in the LSMO/PMN-PT structure also exhibits strong temperature dependence. Our research provides an energy efficient way to design the devices for nonvolatile information storage.

Chapter 2

Background

2.1 Correlated electronic materials

Electronic materials sometimes exhibit strongly correlation among different degrees of freedom with each other. They build a system with novel functionalities. The interactions between electronic spins, charges, orbitals and the lattice induce emergent phenomenon which are different with the individual elements [39]. For example, it is believed to be one of the key issues to understand the systems of high temperature superconductivity, colossal magnetoresistance, magnetoelectric coupling and metal-insulator-transfer. Magnetic perovskites are ideal candidates because they exhibit abundant physical properties based on the transition-metal ion insides an oxygen octahedral cage. The interactions between electrons produce a rich phase diagram which is related to electron hopping and the density of charge carries. The two factors determine the system properties: ferromagnetic or antiferromagnetic, conducting or insulating.

Perovskites have a nearly cubic structure with the general formula $ABO_{3-\delta}$ including an A-site cation, a B-site transition metal and oxygen ions forming corner sharing octahedra around the B-site ion(Fig 2.1). For the complex perovskite structure, B-site contains two or more different cations, which causes the possibility of ordered and disordered variants.

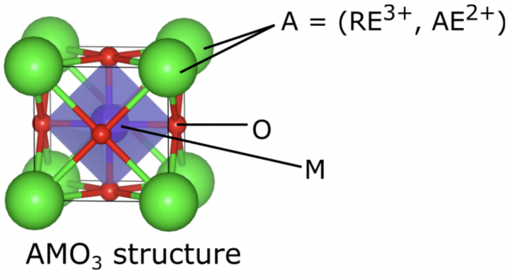

Figure 2.1: Ideal perovskite structure with formula AMO_3 taken from [6]

The relative ion size influences the stability of the perovskite structure. If the coordination numbers of A or B cations are reduced, slight buckling and distortion can produce several lower-symmetry distorted versions. The structure will be transferred to pseudocubic structure or rhombohedral perovskite. Off-centering of an undersized B cation within its octahedron attains a stable bonding pattern, which causes the electric dipole responsible for the ferroelectric property. The A-site of the perovskite can be doped with electrons or holes and governs the increase or decrease of charge carriers density.

Perovskites can also be deposited as epitaxial thin film on other perovskites substrate easily [49]. Due to mismatch strain, charge interaction or compositional changes, new properties can arise.

2.2 Magnetism in transition metal oxides

2.2.1 Crystal field splitting

The electrons of transition metal oxides in 3d orbital are energetically favourable to align in one site ferromagnetically. In the perovskite structure, ferromagnetic ions are surrounded by oxygen octahedra or tetrahedra, which cause the splitting of the 3d orbitals into e_g and t_{2g}. The crystal field energy E_{CF} depends on the distance between transition metal ions and oxygen ligands to separates the orbitals. In octahedral structure, e_g orbitals, in z^2 and $\mathrm{x}^2 - \mathrm{y}^2$ are oriented along the metal-oxygen bond, while the t_{2g}, in xy, xz and yz along between metal-oxygen bonds. The energy of e_g orbitals is increased by $\frac{3}{5}E_{CF}$ and t_{2g} is decreased by $\frac{2}{5}E_{CF}$ because of the Coulomb repulsion. The electrons tend to fill the lower lying level dependent on the crystal field energy E_{CF}. According to the Hund's coupling E_{HR} the occupancy of electrons favours a parallel alignment of all spins. So for the $3d_5$ system in an octahedral environment, if $E_{HR} > E_{CF}$, the electrons are in the same spin state with high spin state S=$\frac{5}{2}$, whereas for $E_{HR} < E_{CF}$, the electrons occupy the low lying t_{2g} firstly with a low spin state S=$\frac{1}{2}$. The splitting is shown in Fig2.2 [34].

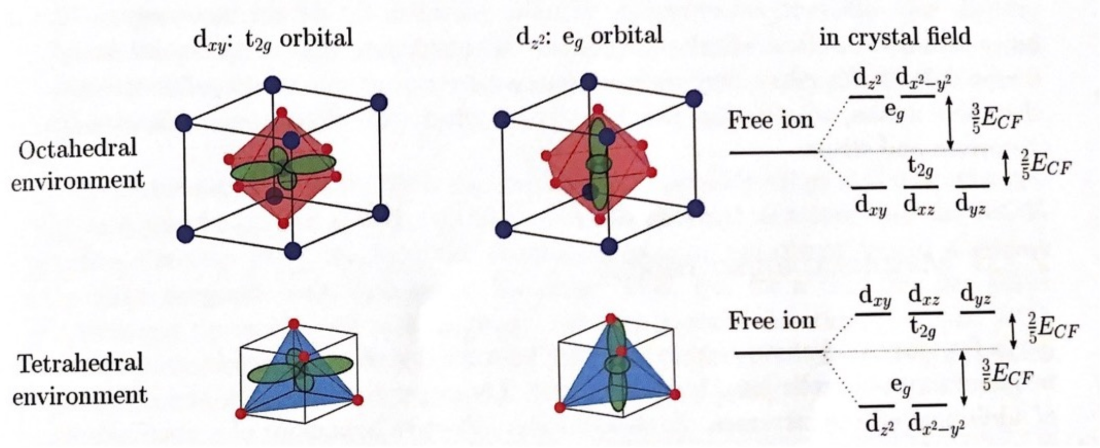

Figure 2.2: Crystal field splitting in octahedral and tetrahedral environment. 3d metal ions are black spheres, the red shaded are oxygen octahedra and cyan shaded the oxygen tetrahedra. The d_{xy} and d_z^2 orbitals are indicated in green. The diagram is taken from [34].

Strain in crystal can cause further degeneracy of orbitals. For an epitaxial thin film grown on the substrate, the stain is produced in the interface due to the mismatch so the bonding along the out-of-plane axis is different from that along the in-plane axis. The degeneracy for orbitals with different z-component is broken. This is explained in Fig 2.3.

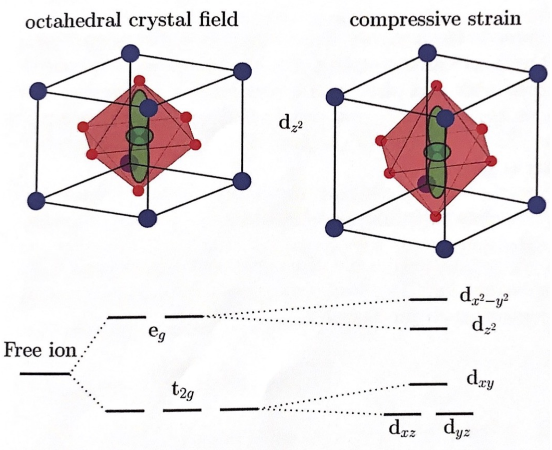

Figure 2.3: Crystal field splitting in octahedral environment and further splitting by compressive strain. The diagram is taken from [34].

2.2.2 Exchange interactions

In transition metal oxides, the 3d magnetic ions are non-neighbouring so the exchange interactions are mediated by the oxygen atoms between them. Two forms of exchange interactions are dominant, double exchange and super-exchange. O^{2-} is highly electronegative with the antiparallel spins in 2p orbitals due to Pauli repulsion, therefore it is magnetically inert. Hence, the oxygen orbitals can exchange directly with 3d metal orbitals as the mediation between metal ions.

Super-exchange occurs in the 180° angle and both half filled 3d orbitals. The valency of two magnetic ions are same. The spins of 3d metal are aligned antiparallel to lower the energy by delocalization. So the super-exchange is usually antiferromagnetic. But if one 3d orbitals is half filled and the other one is either empty or full, or the angle of the two half filled 3d orbitals is 90°, super-exchange is ferromagnetic. The superexchange process is shown in the Figure2.4.

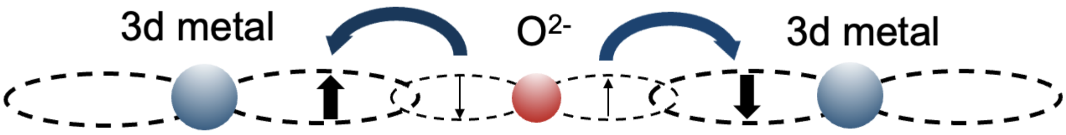

Figure 2.4: Schematic of super-exchange between two 3d metal ions of same valency. The spins of the 3d metal are aligned antiparallel due to a lowering in energy by delocalization.

For double exchange, the 3d metals are in different valency, e.g. in a $Mn^{3+} - O - Mn^{4+}$ configuration in LSMO. The additional electron in t_g level of 3d orbital of the Mn^{3+} cation can hop onto the 2p orbital of oxygen anion, then the oxygen ion in 2p orbital transfers to the the Mn^{4+} in t_g level of the 3d orbital. This is shown in Fig2.5. Since the 2p electron can transfer to the Mn^{3+} only if it is aligned parallel to the electron hopping from the Mn^{3+}, double exchange causes ferromagnetic alignment of the Mn ions.

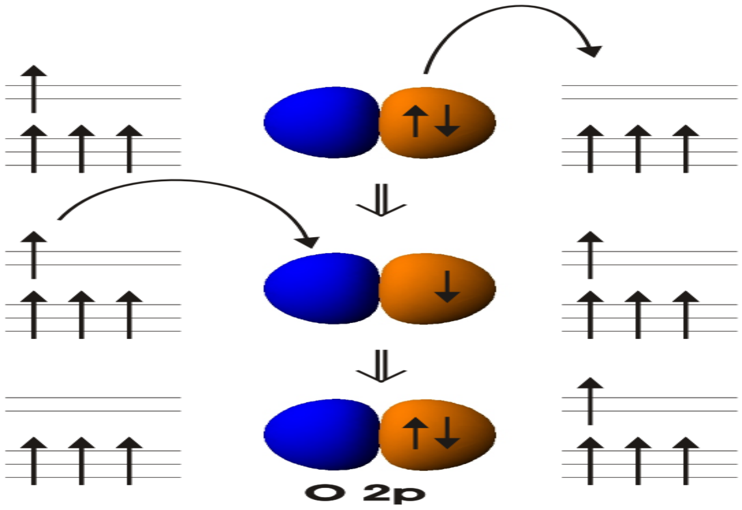

Figure 2.5: Double exchange interaction taking place in Mn-O-Mn bond.

2.2.3 Magnetic anisotropies

Magnetic anisotropy describes the magnetic materials exhibit the different properties in different directions. The interaction of forces between electrons will align the orientation of magnetisation in one direction. The energy density for magnetization to lie along an easy axis is expressed as

$$E_{an} = K_1 sin^2\theta \tag{2.1}$$

with the angle between the magnetization and the anisotropy axes θ and constant K_1. There are three main types of anisotropy: shape anisotropy, magnetocrystalline anisotropy and induced anisotropy, such as strain state.

In thin films, the long-range dipolar interaction influences the shape anisotropy a lot by trying to align the magnetisation in the out-of-plane direction of the film. The dipolar energy density is given by:

$$E_{ms} = \frac{1}{2}\mu_0 M_s^2 cos^2\theta \tag{2.2}$$

with saturation magnetization M_s and the angle between the magnetization and plane normal θ. In this way, the easy and hard directions are created. The magnetization of a thin film is often in-plane with minimal energy.

The magnetocrystalline anisotropy is dependent on the crystalline symmetry. The crystal field interaction and spin-orbit coupling contribute to the anisotropy together. The crystal field leads to easy and hard axes of magnetisation. In cubic systems, the energy density can be expressed by

$$E_{mc} = K_1(sin^2\theta sin^2 2\phi + cos^2\theta)sin^2\theta \tag{2.3}$$

where θ is the angle between magnetisation and z-axis, ϕ is the angle between magnetisation and x-direction. The shape anisotropy and crystalline anisotropy are interplay shown in the thin film structure.

The strain state can also produce the anisotropy, which is same with the orbital degeneracy under strain. The deformation of the unit cell changes the atomic distances and make certain directions favourable. The magnetostriction energy can be given by,

For isotropic in-plane strain:

$$E_{ms} = -\frac{3}{2}\lambda\sigma sin^2\theta \tag{2.4}$$

For anisotropic strain:

$$E = -\frac{3}{2}\lambda_x\sigma_x sin^2\theta cos^2\phi - \frac{3}{2}\lambda_y\sigma_y sin^2\theta cos^2\phi \tag{2.5}$$

in which $\lambda_{x,y}$ is the saturation magnetostriction constants and the $\sigma_{x,y}$ is the strain along the crystallographic axis, θ is the angle between surface normal in z-direction and magnetisation, ϕ is the angle between x-direction and magnetisation [26].

2.3 Magnetoelectric coupling

Magnetoelectric effect reveals the coupling between magnetization and electric polarization in a narrow sense. The magnetization can be manipulated by switching electric field or vice versa. ME coupling can be explained by expansion of free energy which can be given by [12]

$$F = F_0 + E(P - \frac{1}{2}\epsilon_0\chi_e E) + \mu_0 H(M - \frac{1}{2}\epsilon_m H) - \alpha EH - \beta EH^2 - \gamma E^2 H - \sigma E^2 H^2 + ... \tag{2.6}$$

The free energy is the sum of electric displacement, magnetic induction and magnetoelectric coupling. In the equation: F_0:free energy P:Polarisation E,H:electric and magnetic fields ϵ_0:permittivity of free space μ_0:vacuum permeability ϵ_m, ϵ_e:magnetic and electric susceptibility α, β, γ:magnetoelectric coupling coefficients

The first two terms describe the direct interaction between electric and magnetic fields with the electric displacement and magnetization. The terms containing electric field and magnetic field govern the cross-coupling between electric field with magnetisation and magnetic field with polarisation. They describe the interaction between electric field and magnetic field with the electric displacement and magnetisation.

In magnetoelectric coupling term, αEH describes direct magnetoelectric coupling, while the forth term, σE^2H^2 is the strain mediated coupling leading to bigger ME effects.

Direct magnetoelectric coupling only occurs in the system breaking both time inversion and space inversion symmetry.

The polarization can be given by differentiating equation2.6 with respect to electric field

$$P = \alpha H + \beta H^2 + 2\gamma EH + 2\sigma EH^2 + ... \tag{2.7}$$

And magnetization by differentiating equation2.6 with respect to magnetic field

$$M = \alpha E + 2\beta EH + \gamma E^2 + 2\sigma E^2 H + ... \tag{2.8}$$

If an antiferromagnetic system is also ferroelectric, the electric dipole can cause the spin tilting, distorting the antiferromagnetic spin order and arisen magnetic moment [39]. Dzyaloshinskii -Moriya effect describes the ME coupling by mathematical description [35]

$$E_{DM} = \vec{D} * [\vec{S_1} \times \vec{S_2}] \tag{2.9}$$

which reveals the bilinear magnetoelectric coupling. This coupling makes the voltage controlled magnetization possible for memory devices. However, the magnetization arising from the spin tilting is quit weak in single compound magnetoelectrics thereby the artificial multiferroelectric heterostructure is applied.

The ME heterostructure consisting of ferromagnetic and ferroelectric elements aroused great interest for their rich coupling mechanisms. There are two main physical mechanisms playing the role in the ME coupling in such architecture: strain mediation which describes the influence of ferroelectric polarization state on modification of electronic structure at the interface of ferromagnet and the exchange interaction between a ferromagnet and a multiferroic. The magnetization in easy axis is determined by the minimization of the total free magnetic energy F, which can be calculated by the sum of magnetocrystalline energy F_{mc}, the demagnetization energy F_{demag} and the surface or interface magnetic energy $F_{surface}$. Therefore in the FE/FM heterostructure, the term related to magnetoelastic energy is corresponding to the voltage induced strain effects on the magnetic properties. The $F_{surface}$ is related to the electronic effects at the interface. By applying the electric field, the direction of magnetic easy axis can be changed by the generation of large magnetoelectric energy [5].

2.3.1 Strain-mediated ME

Strain mediated coupling is more common in thin film heterostructure, which is dependent on the electrostriction and magnetostriction. Electrostriction refers to electric field manipulation of the change of shape, whereas the magnetostriction corresponds to expansion or contraction of a ferromagnetic material in response to an applied magnetic field [39]. The strain can be transferred from a ferroelectric layer to a ferromagnetic layer. When the electric field applied on a ME heterostructure, the FE material deforms due to inverse piezoelectric effect and generates strain transferred to the deposited FM layer. The strain induced in FM layer can arise in change of coercive field(H_c) and magnetic anisotropy [36].

The strain is the collective effect of elastic deformation and ferroelectric/ferroelastic switching. Strain-electric field curve moves downwards as the elastic deformation. Thereby, at higher stress level the significant switching contribution results in the increase of H_c. The switching is related to 71° or 90° polarization domain switching and they maintain their switched state until enough electric field is applied to overcome the stress state to recover the polarization [17]. The tensile strain and compressive strain is produced in FE/FM heterostructure as shown in Fig2.6(a). The corresponding butterfly curve depicts the strain change via electric field for LSMO/PMN-PT(001) system(Fig2.6(b)).

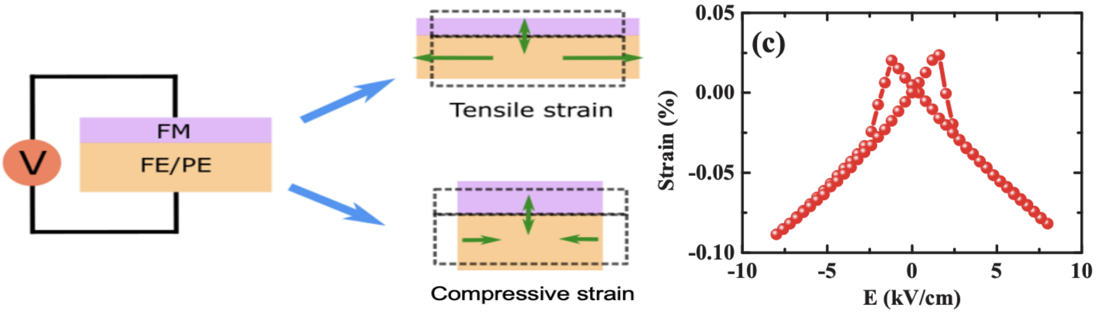

(a) (b)

Figure 2.6: (a)Schematic of strain coupling in a FE and FM heterostructure (b) butterfy-shaped curve characteristic of in-plane piezoelectric strain vs electric feld taken from [43]

2.3.2 Charge-mediated ME

Charge-mediated coupling is relevant to charge carrier density at the interface. When electric field is applied, the bound charges at the ferroelectric interface vary the charge distribution in the ferromagnetic layer. Charge-mediated coupling is based on the Thomas-Fermi screening length in the ferromagnetic materials and change from few Angström to one Nanometer. In the complex ferromagnetic oxide coupled with the ferroelectric materials the charge accumulation can be observed at the interface thereby change the charge doping in ferromagnetic oxide [11]. The charge-mediated coupling is related to non-volatile effects as a result of the performance of remanent polarization in ferroelectric layer giving rise to change in magnetization, which remains stable even after removing the applied electric field.

When applying the electric field, the spin imbalance is enhanced in the ferromagnetic layer thereby magnetic moments are modified [48]. The electronic phase of the magnetic layer is altered such as from ferromagnet to paramagnet or from ferromagnet to antiferromagnet [41]. Meanwhile, different density of states near Fermi-level under different polarizations change the magnetic anisotropy [18]. That is the process of charge-mediated electric field control of magnetism.

2.4 Properties of substrate and thin films

2.4.1 Piezoelectricity and Relaxor Ferroelectrics

Piezoelectric property refers to the electric charges accumulation in response to applied mechanical stress in crystal. The piezoelectric effect is a reversible process that internal strain induced by the applied electric field, which is called ”inverse piezoelectric effect”. All ferroelectrics are piezoelectrics(PE) but not all piezoelectrics are ferroelectrics. When the crystal is in an equilibrium state, the internal electric charges are balanced. On application of mechanical stress, atoms are accumulated or separated which alters the balance of electric charges and the electric dipoles are created. Therefore, positive and negative charges appear on the surface of crystal.

The relaxor ferroelectric properties(RFE) are also relevant. The normal ferroelectrics can transfer to the relaxor ferroelectrics with increasing disordered component on crystal lattices. The disordered ferroelectrics comprise of randomly distributed polar nanoregions with different directions of electric dipole moments in separated domains [45]. These domains orient themselves with the field producing a large polarization. Most of the domains come back to the random orientation causing a slimming down of the hysteresis loop compared to classical ferroelectric [46].Relaxor ferroelectrics are characterized by three temperatures: Burns temperature T_B at which polar nanoregions start appearing, intermediate temperature T_{im} when polar nanoregions become stable and permanent and T_c which is from cubic to tetragonal phase transition [40]. RFE follows the temperature dependence permittivity as below:

$$1/\epsilon \propto (T - T_0)^2 \tag{2.10}$$

Whereas the normal ferroelectrics follow Curie-Weiss law and T_0 is Curie-Weiss temperature,

$$1/\epsilon \propto (T - T_0) \tag{2.11}$$

Relaxor ferroelectric property shows a broad-diffuse phase transition around maximal Curie temperature and strong frequency dependence [47]. The origin of the diffuse phase transition based on local compositional fluctuations associated with B-site cation disorder results in a distribution of Curie temperature.For example, PMN-PT with an overall close-to-cubic structure forms some nanoregions due to the disorder of B-site cation in different size and valency(e.g. Mg^{2+} and Nb^{5+}) while under a critical temperature T_B. There are two models explaining the existence of nanoregions, one is that the nanoregions are separated by the domain walls, the other is the regions are in small domains within a cubic matrix.

2.4.2 $[Pb(Mg_{1/3}Nb_{2/3})O_3]_{1-x}$-$[PbTiO_3]_x$(PMN-PT)

The structure of PMN-0.3PT corresponds to $A(B'B'')O_3$ in which B-site is shared by Mg^{2+} and Nb^{5+}. It exhibits excellent piezelectric and ferroelectric properties based on perovskite structure with cubic symmetry. On applying an electric field, the Pb and Nb can displace easily without causing any distortion to the oxygen framework and large polarization can be produced. The displacement of both Pb and Nb goes along $< 111 >$ direction and the magnitude of Pb displacement is enhanced as the Mg/Pb ration increases. The displacement correlations are formed as nano-regions below Burns temperature. These polar nanoregions have nonzero spontaneous polarization. The bond between Pb^{2+} and oxygen, Nb^{5+} and oxygen are short but strong covalent bonds due to the hybridization whereas for low ionic charge of Mg^{2+}, the force of covalent bond between Mg and oxygen is less, which causes the underbonded oxygen atoms. Thereby, large Pb off-centering is needed to meet the oxygen bonding requirements [14].

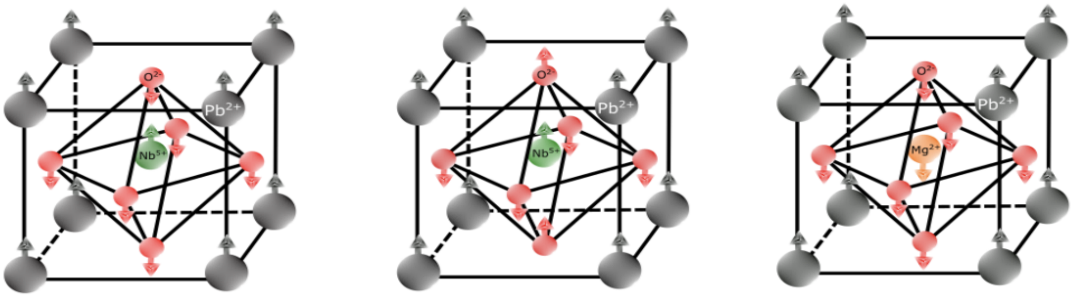

Figure 2.7: Cation-oxygen displacement modes (inspired from [14].

The Pb and Nb displacement is opposite to oxygen and Mg is positively correlated with oxygen as shown in Figure 2.7. By replacement of Mg^{2+}/Nb^{5+} with Ti^{4+} at B-site, the relaxor properties can be reduced and the Curie Temperature can be increased above room temperature [44]. A new ferroelectric phase near morphotropic phase boundary appears which divides the relaxor side(pseudocubic) and ferroelectric side(tetragonal). As a result, PMN-30%PT shows pseudocubic structure on average. It was observed that in 0.7PMN-0.3PT, the spontaneous polarization decreases but not vanishes with the increase in temperature. Therefore, the ferroelectric and paraelectric phase coexist on microregions near the transition temperature.

At room temperature, PMN-0.3PT is rhombohedral with pseudocubic structure with lattice constant a=4.02$\mathring{A}$ and angle $\alpha = \beta = \gamma = 89.90°$. They have eight possible polarization directions along $< 111 >$ and three types of domain switching: 71°, 109°(ferroelastic) and 180° (ferroelectric).The total polarization can be calculated by adding the two phase PMN and PT [21]:

$$P^{total} = P_r^{Ti} x^{PT} + P_r^{PMN} x^{PMN} \tag{2.12}$$

P_r^{Ti} and P_r^{PMN} are polarization values of PT and PMN phases.

Different crystal cuts can produce different surface orientations of PMN-PT. In PMN-PT(001), [001] direction is out-of-plane, [100] and [010] are equivalent in-plane directions. All polarisations along $< 111 >$ are equivalent so the strain are cancelled out with each other. The polarisation vectors with an out-of-plane component antiparallel to the field and they try to align with the field by applying electric field. Thus, tensile strain occurs in crystal. The polarisations will not disappear after removing the voltage until the coercive field is applied. The tensile strain is released. Then as the increasing voltage, the compressive strain is created. The switching process is also exhibited in polarization and strain loop.

For PMN-PT(111), two in-plane directions [-110] and [11-2] are crystallographically distinct and exhibits drastically different behaviour in electric field. Polarizations perpendicular to (111) plane is distinct with others as shown in Figure2.8(Polarization varients r1 in purple arrows). Compared to the (001) plane, there is a remanent compressive strain present after removing an applied electric field due to the out-of-plane polarizations.

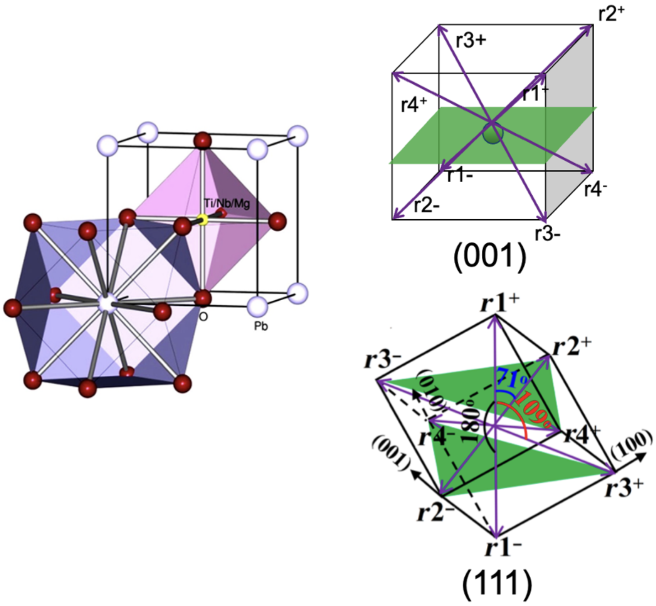

Figure 2.8: PMN-PT structure in (001) and (111) plane(inspired from [14].

2.4.3 $La_{0.7}Sr_{0.3}MnO_3$(LSMO)

LSMO is the Sr-doped $LaMnO_3$ single crystal with complex structure and orbital degrees of freedom, which accounts for lattice,charge and spin coupling. Different Sr doping exhibits different magnetic phases as shown in the phase diagram [20].

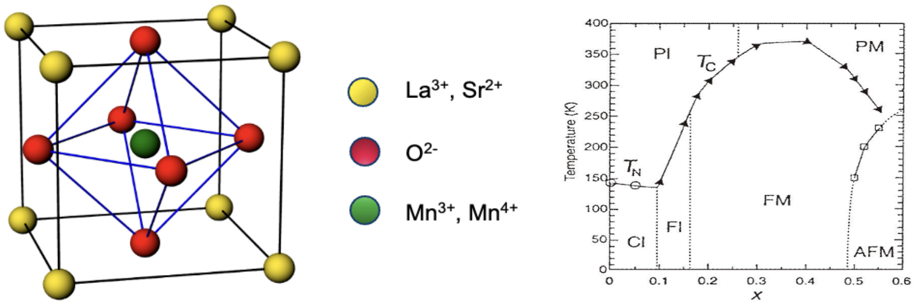

(a) (b)

Figure 2.9: (a)$La_xSr_{1-x}MnO_3$ structure (b)$La_xSr_{1-x}MnO_3$ phase diagram reproduces from [20].

In my work I use the Sr-doping x=0.3($La_xSr_{1-x}MnO_3$) and it shows the semi-metallic ferromagnetism in room temperature. The Curie temperature is 370K. With increasing Sr content, the holes in Mn site are generated by replacing La^{3+} ions. The (1-x) Mn^{3+} and x Mn^{4+} are produced to ensure the charge neutrality. Double exchange arising from the mixed valence states of Mn^{3+} and Mn^{4+} causes the ferromagnetic ordering.

2.5 Scattering theory

In order to investigate the microscopic structure of crystals and its physical properties non-destructively, scattering methods are very useful.

The basic scattering theory is based on the de-Broglie relation which describes a particle beam as wave [10, 37]. The incident wave vector is $\vec{k}$ and the scattered wave is $\vec{k}'$. In the elastic scattering,the relationship is :

$$|\vec{k}| = |\vec{k}'| = \frac{2\pi}{\lambda} \tag{2.13}$$

The plane wave emitted from source hit the sample and the scattered plane wave earned at the detector. The scattering vector which describes the in and out wave can be described as,

$$\vec{Q} = \vec{k}' - \vec{k} \tag{2.14}$$

The magnitude of the scattering vector is calculated with the wavelength λ and scattering angle θ as

$$Q = |\vec{Q}| = \sqrt{\vec{k}^2 + \vec{k}'^2 - 2\vec{k}\vec{k}'cos2\theta} = \frac{4\pi}{\lambda}sin\theta \tag{2.15}$$

X-rays, also called the electromagnetic radiation are scattered by the electrons in atoms through the interaction of the electric field and the polarisability of the atom. In my thesis, X-Ray reflectometry and diffraction are mostly used.

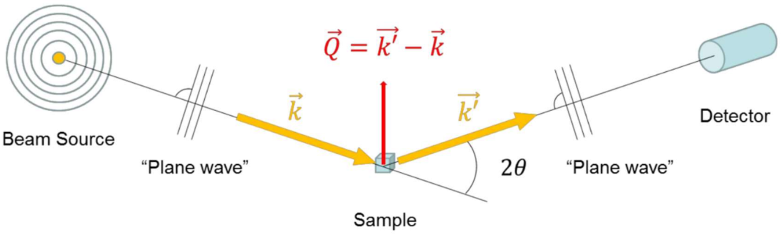

Figure 2.10: Scattering in the Fraunhofer diffraction approximation.Figure taken from ref [10]

2.5.1 X-ray Reflectometry

X-ray reflectometry is a surface sensitive characterization method to investigate the surface and interface in thin films. The incident beam is partially reflected at the incident angle and partially transmitted under a different angle due to the refraction. The total reflection is generated below a critical angle θ_c, which is defined as:

$$\theta_c = cos^{-1}n \cong \lambda\sqrt{\frac{\rho}{\pi}} \tag{2.16}$$

with the index of refraction n slightly smaller than 1 for most materials, λ and ρ represent the wavelength and the electron density for X-rays.

For the thin film thickness d, the constructive interference occurs when the Bragg equation is satisfied. This leads to the constructive interference between beams reflected from the surface of the thin film and interface between layer and substrate, which is called "Kiessig fringes", an oscillatory pattern of the intensity. The thickness can be measured by the two maximal distance, δQ [22],

$$d = \frac{2\pi}{\delta Q_{Kiessig}} \tag{2.17}$$

If the interfaces are not perfectly flat, the roughness, σ_x, for the layer x, distributes the height and leads to the decay of reflectivity.

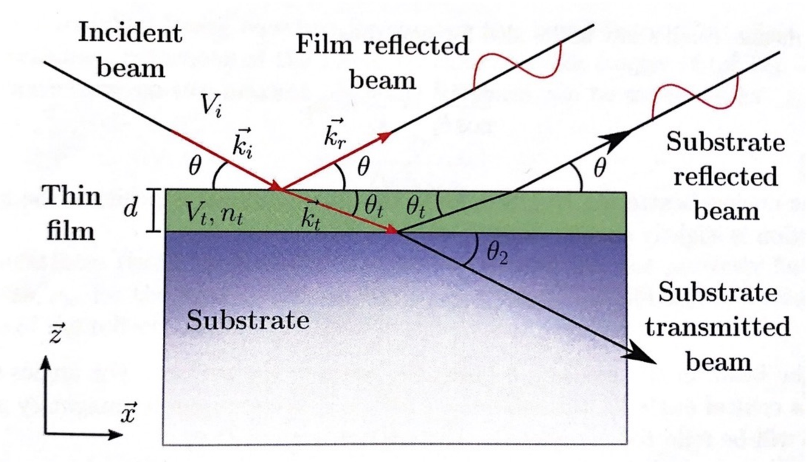

Figure 2.11: Scattering from a thin film sample for a reflection condition. The beam reflected from the film and substrate acquire a phase difference, which results in Kiessig fringes due to constructive and destructive interference for varying incidence angle.Image adapted from [22].

2.5.2 X-ray Diffraction

In a crystal, at each lattice point the basis is repeated. The set of atoms repeat at every lattice point and builds up the crystal lattice. Thus, the crystal exhibits a large number of symmetries based on the lattice and basis. In X-ray diffraction, the crystal exhibits a periodic pattern correlation with the crystal structure.

The point lattice is indicated by the lattice vectors a, b and c and angles between a, b and c are α, β and γ. The crystal shows different lattice for different relationship between lattice constant and angles. The direction of the vector is $[uvw]$. A set of parallel lattice planes are defined by the Miller indices (hkl). The distance between the lattice planes, $d(hkl)$ in orthorhombic lattice is described by:

$$d(hkl) = \sqrt{(\frac{h^2}{a^2} + \frac{k^2}{b^2} + \frac{l^2}{c^2})} \tag{2.18}$$

The diffraction is based on the Fourier transform of a crystal lattice. So we use the reciprocal lattice vector to define the reciprocal lattice.

$$\vec{G} = h\vec{g_1} + k\vec{g_2} + l\vec{g_3} \tag{2.19}$$

for the real space vector $\vec{R} = u\vec{a_1} + v\vec{b_2} + w\vec{c_3}$

in which

$$\begin{aligned}
\vec{g_1} &= \frac{\vec{b}\times\vec{c}}{\vec{a}\cdot(\vec{b}\times\vec{c})} & \vec{g_1}\cdot\vec{a} &= 2\pi & \vec{g_1}\cdot\vec{b} &= \vec{g_1}\cdot\vec{c} = 0 \\
\vec{g_2} &= \frac{\vec{a}\times\vec{c}}{\vec{a}\cdot(\vec{b}\times\vec{c})} & \vec{g_2}\cdot\vec{b} &= 2\pi & \vec{g_2}\cdot\vec{a} &= \vec{g_2}\cdot\vec{c} = 0 \\
\vec{g_3} &= \frac{\vec{a}\times\vec{b}}{\vec{a}\cdot(\vec{b}\times\vec{c})} & \vec{g_3}\cdot\vec{c} &= 2\pi & \vec{g_3}\cdot\vec{a} &= \vec{g_3}\cdot\vec{b} = 0
\end{aligned} \tag{2.20}$$

For one dimension, the intensity of the scattering is given by the square of the amplitude as,

$$I(\vec{Q}) = |A(\vec{Q})|^2 = |b|^2 \frac{sin^2(1/2NQ_c)}{sin^2(1/2Q_c)} \tag{2.21}$$

The maximum intensity is at $\frac{1}{2}Q_c = j\pi$ for an integer j. In Bragg equation,

$$Q_{Bragg} = j\frac{2\pi}{c} \tag{2.22}$$

For three dimension the constructive interference is given by:

$$\vec{Q}\cdot\vec{R} = 2\pi j \tag{2.23}$$

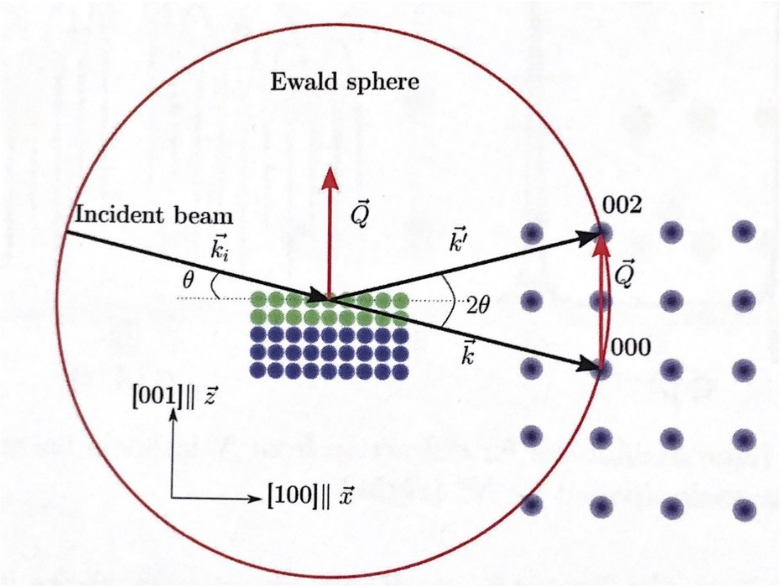

Figure 2.12: Ewald construction for diffraction from a thin film sample.Image taken from [34].

According to the definition of the reciprocal lattice, Laue condition is satisfied when

$$\vec{Q} = \vec{G} \tag{2.24}$$

which can be exhibited in Ewald construction in Fig 2.11. The $\vec{k}$ is from the sample to the origin of the reciprocal lattice. The radius of the Ewald sphere is $|\vec{k}| = 2\pi/\lambda$. If $\vec{k'}$ lies on a reciprocal lattice point, $\vec{Q} = \vec{G} = \vec{k'} - \vec{k}$ conforms to Laue condition. By measuring the intensity in corresponding position, the reciprocal space map can be plotted(Fig 2.11).

The diffraction gives information about the crystalline structure including the interplane spacing and the number of crystalline layers. By measuring the lattice constant of substrate and film, the strain state can be investigated.

Chapter 3

Experimental methods and instruments

3.1 Sample preparation

3.1.1 High Oxygen Pressure Sputtering Deposition(HOPSD)

High Oxygen Pressure Sputtering Deposition(HOPSD) is one of the main deposition method to grow epitaxial thin film $La_{0.7}Sr_{0.3}MnO_3$ on PMN-PT substrate. The growth process works under oxygen plasma generated by 13.6MHz radio frequency. The target atoms are sputtered and ejected by bombardment of negatively charged oxygen ions from oxygen plasma. Then the ejected atoms or clusters move towards the substrate in stoichiometry and experience surface diffusion, nucleation and growth on the substrate to form the thin film.

The deposition process of HOPSD is at high oxygen pressure of 1-4 mbar, leading to a short mean free path of target materials as well as the localization of plasma. It is helpful for suppressing the back-sputtering effects of the deposited layer. Besides,the large oxygen pressure ensures a low oxygen vacancy concentration during the growth process. In this way, HOPSD can fabricate a metal-oxides thin film with better quality.

The vacuum in the range of 10^{-6} mbar is prepared by two-stage pumping system before sputtering. In order to clean the target and substrate from contaminants and enhance the surface diffusion during the growth, the ”Pre-sputtering” process goes on under a desired oxygen (about 2-3 mbar for my sample) and high temperature up to 700°C. The oxygen gas is controlled by mass flow contoller(MFC). Leaving the substrate during the presputtering far away as possible from the targets with unwanted coating is required. In the sputtering growth process, the target is transported right above the substrate with the distance about 2 cm and temperature is kept at 700°C [15].

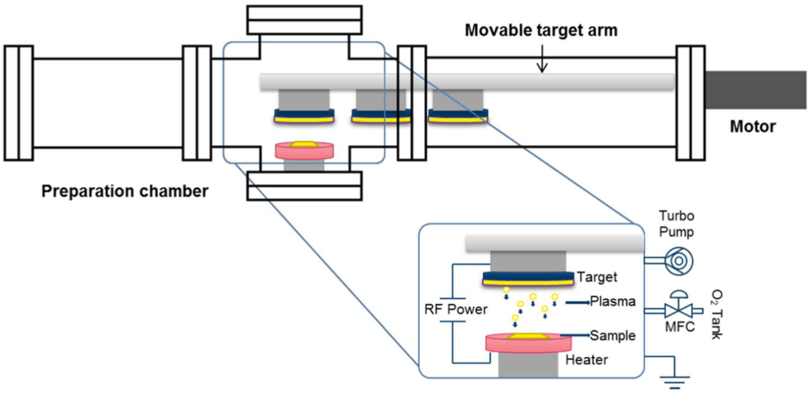

Figure 3.1: Sketch of the HOPSD device.Image taken from [15]. On-axis RF sputtering with a maximum power of 200 W. The target-substrate distance is fixed at 2 cm.

3.2 In-house Characterisation Methods

3.2.1 X-ray reflectometry(XRR) and X-ray diffraction(XRD)

The D8 Advance X-ray reflectometer and X-ray Diffraction from Brucker AXS is used to characterize the out-of-plane crystallinity, thickness and roughness of thin film samples. The schematic geometry structure of set-up is shown in Fig 3.2. The X-ray source is generated by $Cu-K_{\alpha 1}$ with a wavelength of $\lambda = 1.54\mathring{A}$ .For the reflectometry scan, two Göbel mirrors are mounted to ensure a highly collimated beam at low angles.For precise diffractometry scan, a channel cut monochromator is used at high angles [19].

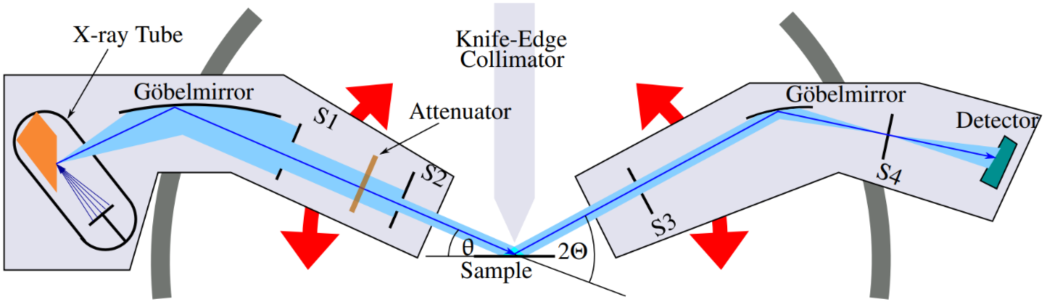

Figure 3.2: Sketch of the Bruker D8 Advance.Taken from [19].

3.2.2 GALAXI:Gallium anode low-angle x-ray instrument

The high brilliance laboratory small angle X-ray scattering instrument GALAXI enables performing GISAXS experiments in reflection at grazing incidence, SAXS experiments in transmission geometry and WAXS(Wide-angle X-ray Scattering) measurement. The X-ray source is generated by METALJET source built by Brucker AXS with GaInSn alloy as anode and its wavelength is $1.34\overset{\circ}{A}$. A schematic geometry of the GALAXI platform is presented in Fig 3.3 [23].

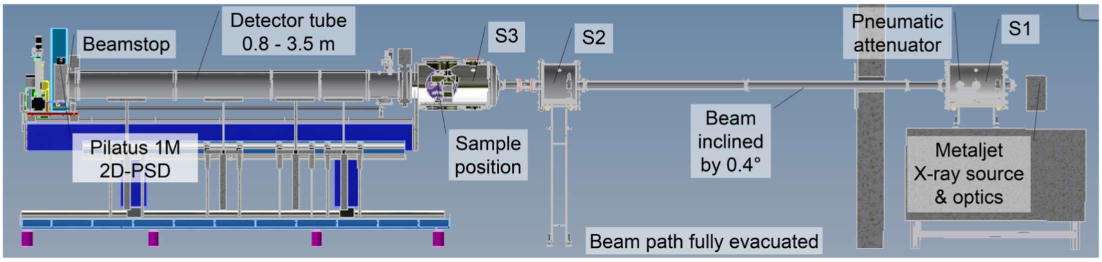

Figure 3.3: Schematic drawing of GALAXI with its main components. The beam direction is from right to left. Image taken from [23].

The sample is mounted at a horizontal rotator in the chamber(Figure3.3), which can be adjusted by two rotational and two translational degrees of freedom. A detector with 64*8 mm^2 active area and 1280 channels is installed at the distance 85cm away from sample and the position can be changed according to different value of 2θ for different lattice faces.

When the sample is rotated by horizontal sample holder, the value of x-ray scattering with a 2θ range between $2\theta_1$ and $2\theta_2$ is recorded at varies ω values in the range of 0° and 360°. According to the Bragg's rule and the relationship between reciprocal lattice and real lattice, at every single angle of ω, the intensities of x-ray diffraction from reciprocal lattice Q_1 to Q_2 are recorded by the detector. Then the entire reciprocal space of the sample can be plotted. As my sample is put in the direction shown in the Figure3.4, the horizontal axis is (110) direction, while the vertical axis is (001) direction. The detailed illustration can be depicted in Figure3.4.

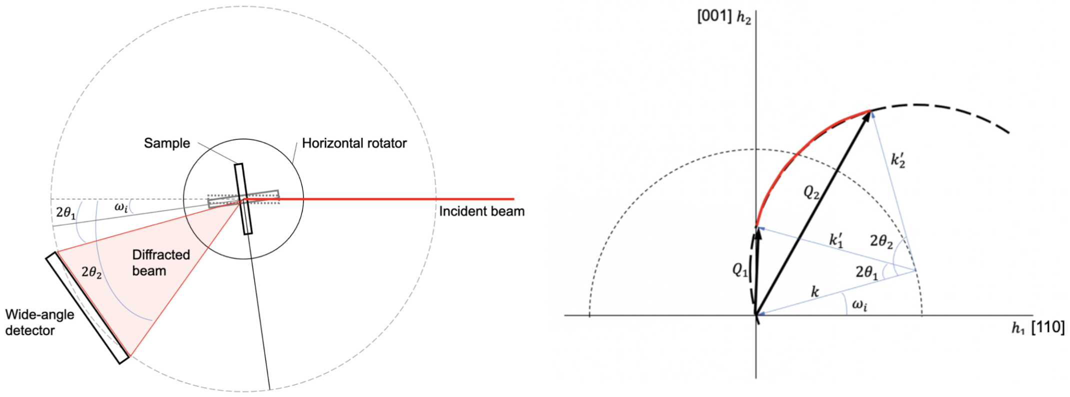

(a)

(b)

Figure 3.4: (a) is the schematic geometry of the WAXS. (b) is the calculation of the reciprocal data from the WAXS data.

3.2.3 Magnetic properties measurement system(MPMS)

The Superconducting Quantum Interference Device(SQUID)-magnetometer from Quantum Design and a superconducting magnet inside a liquid helium Dewar vessel enables measuring the magnetic characterisation [1]. The temperature range from 1.9K to 400K with a field up to 7T is allowed to be measured.

The basic schematic diagram of set-up is in the Figure3.5. The sample is mounted inside a plastic straw and inserted into the MPMS chamber in the helium atmosphere. The magnetic field is generated by the superconducting magnet and along the straw direction parallel to the direction of travel. The sample is moved through the pickup coils made of a superconducting wire, also called a second-order gradiometer [28]. The magnetic moment of the sample induces a current in the coils, which is coupled into the SQUID circuit. A SQUID circuit with a superconducting loop with a Josephson junction measures local changes in magnetic flux density caused by sample motion.The sensitivity of SQUID to small magnetic moments is very high about $5 * 10^{-12} Am^2$ [32, 27].

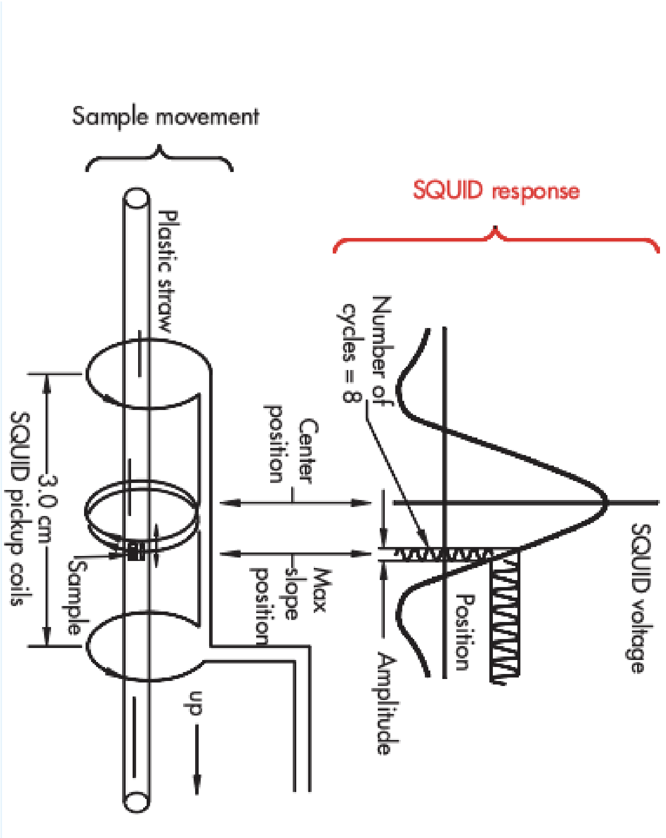

Figure 3.5: Schematic of the MPMS setup.Image taken from [27]

The set-up also can perform the magneto-electric coupling measurement by applying the voltage on the sample based on the design of Borisov et al [8]. The sample is contacted by the two copper wires via silver paste and connected with the voltage source outside the system.

There are two types of movement for the sample, which are DC transport and reciprocating sample option(RSO) [3]. The DC options move the sample gradually through the pickup coils in discrete steps, whereas in the RSO mode the sample oscillate rapidly. The RSO mode is faster and more accurate than the DC option.

3.2.4 Dynamic Hysteresis Measurement

Dynamic hysteresis measurement can be used to measure the ferroelectric properties of materials. The ferroelectric materials exhibit a hysteretic curve of electric polarization versus electric field strength. In the figure of the results, we can get the information from its axis intercepts, representing the remanent polarization and the coercive field.

The basis of the set-up utilized a known resistor in series to the ferroelectric to access the polarization via the displacement current under the dynamic voltage [31]. The polarization is the material related part of the electric displacement field D which also includes the vacuum contribution. D is related to the electric field strength E via the electric constant and relative permittivity ε_r. Moreover, it indicates a charge Q per area A, i.e., an area charge density extracted from the measurement

$$D = D_0 + P = \varepsilon_0 * \varepsilon_r * E = \varepsilon_0 * E + P = \frac{Q}{A} = \frac{\int I(t)\,dt}{A} \tag{3.1}$$

In practice, the difference between D and P is negligible since for a rather low electric displacement field and a rather high electric field, D_0 becomes really low with a relative difference between D and P is less than 1%. For lower polarization and higher fields, the characteristic figure P_r is not affected by the approximation.

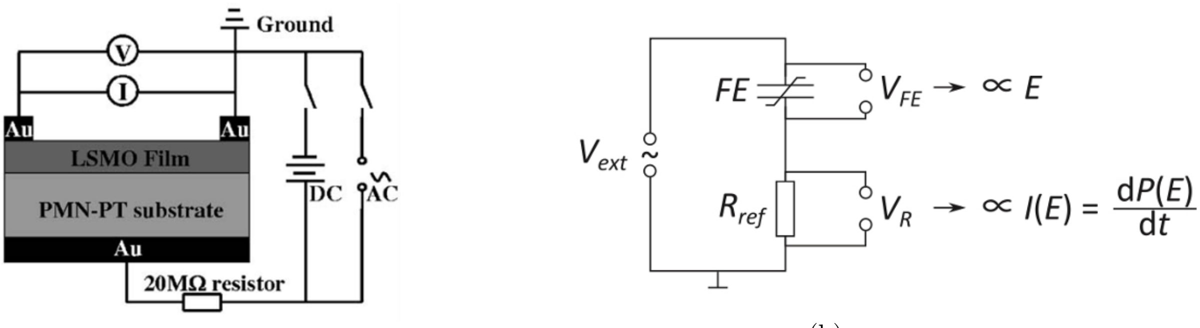

(a)

(b)

Figure 3.6: (a) is the connect for dynamic hysteresis set-up.(b) is the shunt method to explain the principle.Taken from [31].

The current response I(t) of a real ferroelectric to an AC excitation signal E(t) consists of three contributions [29]: (1)dielectric current,(2)ferroelectric switching current and (3)leakage current. The two former depend on the slope of the excitation field (i.e. the frequency and the wave form of the signal), whereas the latter mostly shows an exponential-like dependence on the electric field strength. Leakage current causes a blown up hysteresis with intercepts that deviate to a greater or less extent from the true remanent polarization and coercive field of the ferroelectric.

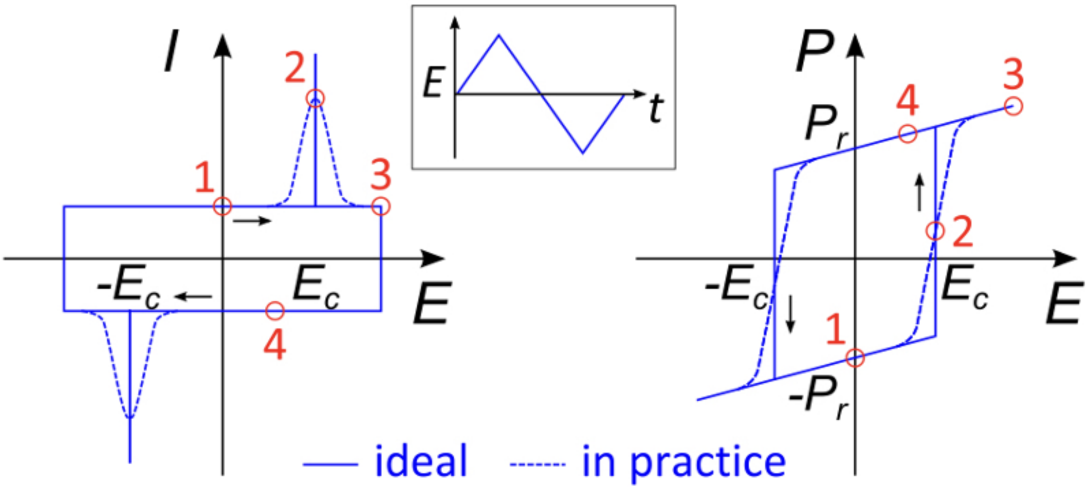

Figure 3.7: Ferroelectric polarization hysteresis (P-E, right) as a result of the transient currents (I-E, left) integrated during a triangular field sweep (inset): (1) linear region around the negative remanent polarization $-P_r$, (2) switching around the coercive field E_c, (3) saturation region, and (4) linear branch towards the positive remanent polarization P_r. The diagrams are taken from [31].

Chapter 4

Results and Discussions

4.1 Growth and Characterisation of LSMO/PMN-PT heterostructure

$[Pb(Mg_{1/3}Nb_{2/3}O_3]_{0.7}$ -$[PbTiO_3]_{0.3}$(PMN-PT) substrates with ferroelectric properties are used for experiments with ferromagnetic thin films. The LSMO thin film with ferromagnetic property is grown by HOPSD on PMN-PT(001) and PMN-PT(111) substrate from Malteck company.

The film quality is determined by growth temperature, oxygen pressure, plasma power and growth time.The basic parameter for growth is listed in the Table 4.1.

Table 4.1: Growth Parameters

Sample	Substrate Size [mm*mm]	Substrate company	Growth temperature [$^\circ C$]	Oxygen Pressure [mbar]	Plasma Power [W]	Growth time [min]
(001)	5*5	Malteck	700	2	90	90
(111)	5*5	Malteck	710	2	90	90

The X-ray diffraction measurement in Figure 4.2 presents the XRD θ-2θ scan pattern of as-grown LSMO/PMN-PT(001) and (111). The two peaks of film and substrate are visible, but the LSMO peak in (111) direction is much weaker than (001). That's because the in-plane lattice arrangement of LSMO unit cell on PMN-PT (001) substrate is different with (001) as shown in Figure4.1. The epitaxy growth thin film on (111) is more difficult than (001) orientation. Therefore, the thin film quality is not so good.

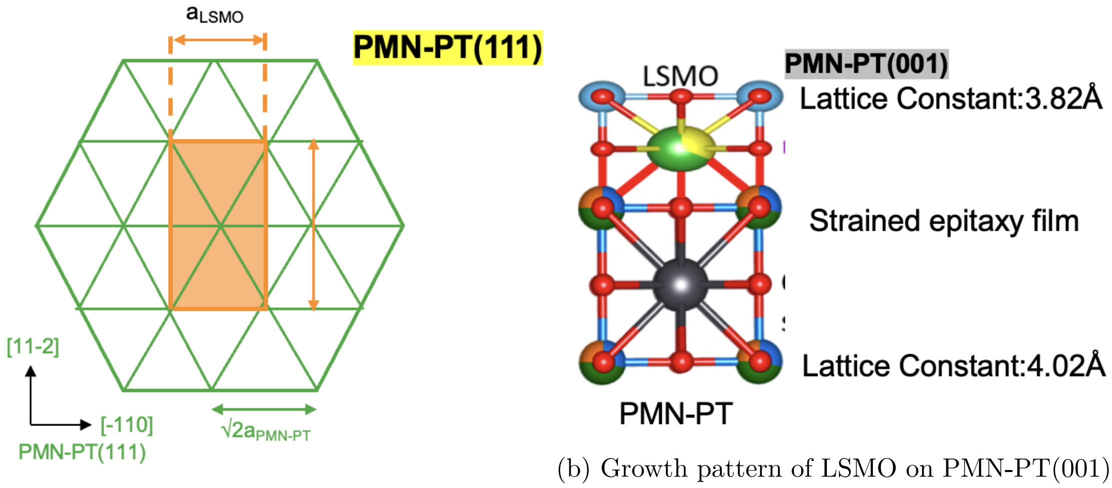

(a) Growth pattern of LSMO on PMN-PT(111)

(b) Growth pattern of LSMO on PMN-PT(001)

Figure 4.1: Schematic growth method for LSMO thin film on PMN-PT(111) plane and (001) plane inspired from [6].

According to Bragg's rule, the calculated out-of-plane lattice constant, d_{111} of LSMO thin film($2.25\mathring{A}$) is smaller than the bulk value($2.269\mathring{A}$). Considering the in-plane lattice mismatch of +3.5% between PMN-PT(001) and LSMO, the reduction of out-of-plane lattice parameter indicates that the LSMO film suffers an in-plane tensile strain and out-of-plane compressive strain.

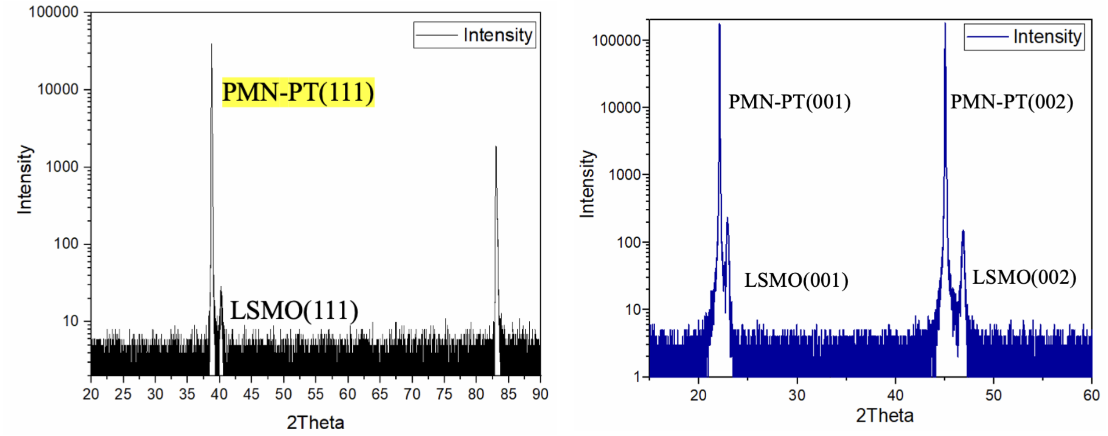

(a) XRD $\theta - 2\theta$ scan along[001]

(b) XRD $\theta - 2\theta$ scan along[111]

Figure 4.2: XRD measurement of sample LSMO/PMN-PT(111) and (001).

Based on X-ray reflectivity measurement the layer thickness was determined by fitting

XRR data using the software GenX. The initial layer and substrate density were taken from the ICSD database [2]. As illustrated in Figure 4.3, the XRR data of sample can be simulated well by adding a top layer with slightly reduced scattering length density when 2θ is smaller than 2°. The thickness of LSMO thin film on PMN-PT(001) is 40.8 nm, on PMN-PT(111) is 38.7 nm, which can be used to normalize the magnetization. Other information from the XRR measurement is presented in Table 4.2 and Table 4.3.

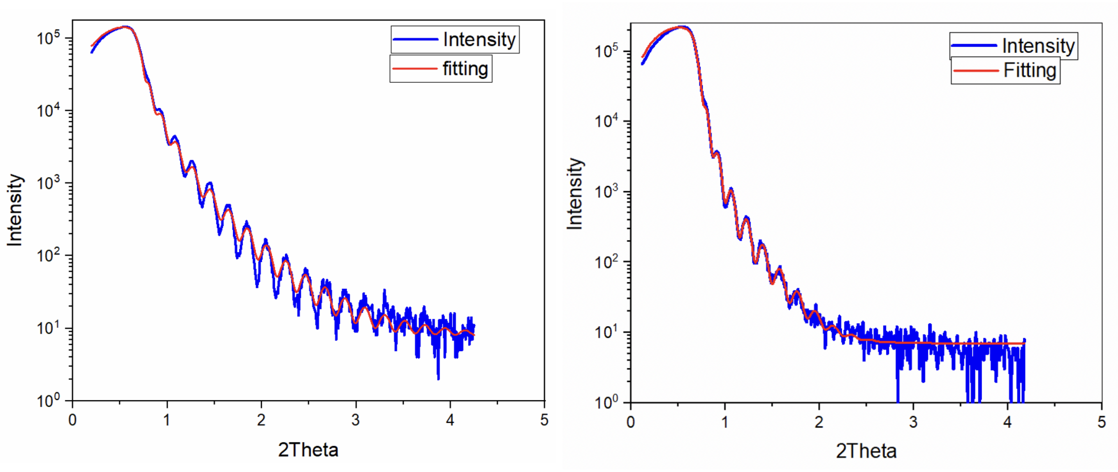

(a) XRR measurement for LSMO/PMN-PT(111)

(b) XRR measurement for LSMO/PMN-PT(001)

Figure 4.3: XRR measurement and scattering length density profile of sample LSMO/PMN-PT(111) and (001).

Table 4.2: Fit of the XRR measurement of LSMO/PMN-PT(111) in Fig4.2

Layer	Thickness[nm]	Roughness[nm]
Top layer	$2.18^{+0.3}_{-0.5}$	$6.14^{+0.06}_{-0.05}$
LSMO	$38.69^{+0.2}_{-0.3}$	$10.11^{+0.4}_{-0.1}$

Table 4.3: Fit of the XRR measurement of LSMO/PMN-PT(001) in Fig4.3

Layer	Thickness[nm]	Roughness[nm]
Top layer	$2.19^{+0.1}_{-0.3}$	$1.06^{+0.02}_{-0.03}$
LSMO	$40.88^{+0.4}_{-0.2}$	$3.29^{+0.5}_{-0.1}$

4.2 Polarization of PMN-PT substrates

In PMN-PT, the electric polarisation vectors within one polar nanoregion are aligned parallel and oriented along $< 111 >$ direction. Upon applying an out-of-plane electric field loop on the sample with LSMO and gold thin film as two electrodes, the polarisation follows a hysteretic behaviour(Fig 4.4). The polarization increases with the electric field until reach the saturated polarization.By removing the voltage,the polarization doesn't return to zero but maintains the saturated state with a slight decrease. The polarisation can return to zero until the negative coercive field is applied.

For PMN-PT(111), the electric field is along the $< 111 >$ direction parallel with one of the polarization variants. Therefore, the polarization variation with electric field for PMN-PT(111) is more sensitive than PMN-PT(001). The saturated polarization is also larger due to the easily rotation of polarzation variants. The hysteresis loop shows a good ferroelectricity with a coercive field of 2.4kV/cm(111) and 1.4kV/cm(001).

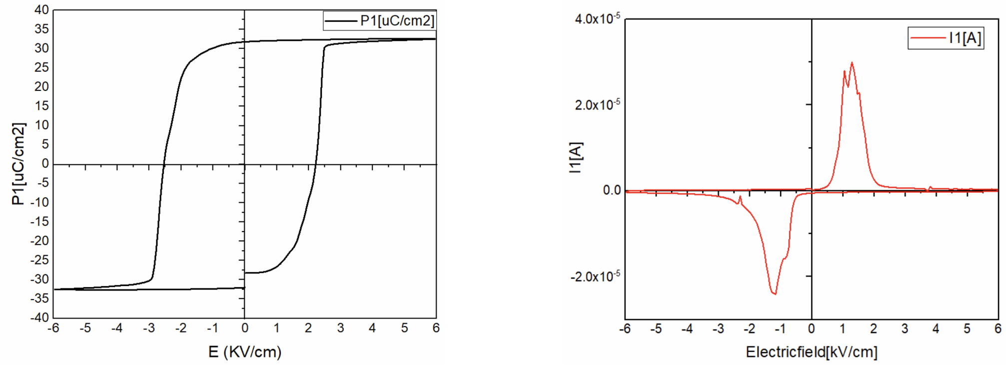

(a) Polarization of PMN-PT(111)

(b) Transient currents of PMN-PT(111)

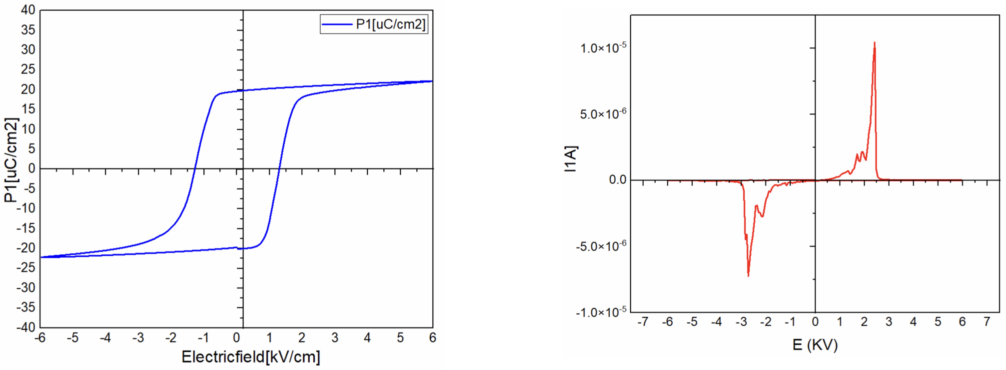

(c) Polarization of PMN-PT(001)

(d) Transient currents of PMN-PT(001)

Figure 4.4: (a)Polarization of PMN-PT(111) at 300K with the maximal electric field 6kV/cm.(b) is the transient currents integrated during a triangular field sweep.(c)Polarization of PMN-PT(001) at 300K with the maximal electric field 6kV/cm.(d) is the transient currents integrated during a triangular field sweep.

4.3 Reciprocal lattice map of PMN-PT substrates

In order to investigate the polarization domain switching in PMN-PT(111) substrate, a x-ray reciprocal space mapping(RSM) technique based on wide-angle-scattering was used to quantitatively determine the polarization switching pathway in response to the electric fields. Figure4.5 shows the RSMs of the PMN-PT(111) substrate in the vicinity of the (222) reflections under various poling states. There are two lines in the RSM and the weaker lines are caused by the $Cu - K_{\alpha 2}$ in the X-ray source. Due to the rhombohedral symmetry in the PMN-PT single crystal, four possible strain states(r1,r2,r3,r4) exist as displayed in Figure4.5(d). According to lattice parameter and rhombohedral domain structure, r1 can be distinguished with others by the different spot distributions and intensities. After a positive electric field was applied on the sample, the RSM in Figure4.5(b) shows a single high intensity reflection spot with a lower Q_{222} value, while the spot with the high Q_{222} value vanishes. This high intensity spot corresponds to the r1 domain states, with all the polarizations pointing to the out-of-plane direction. After a negative coercive electric field is applied, the spot with the distinct lower Q_{222} value disappears as shown in Figure4.5(f), indicating that the polarization variants changing from r1 to r2/r3/r4 undergoes a 71° domain switching.

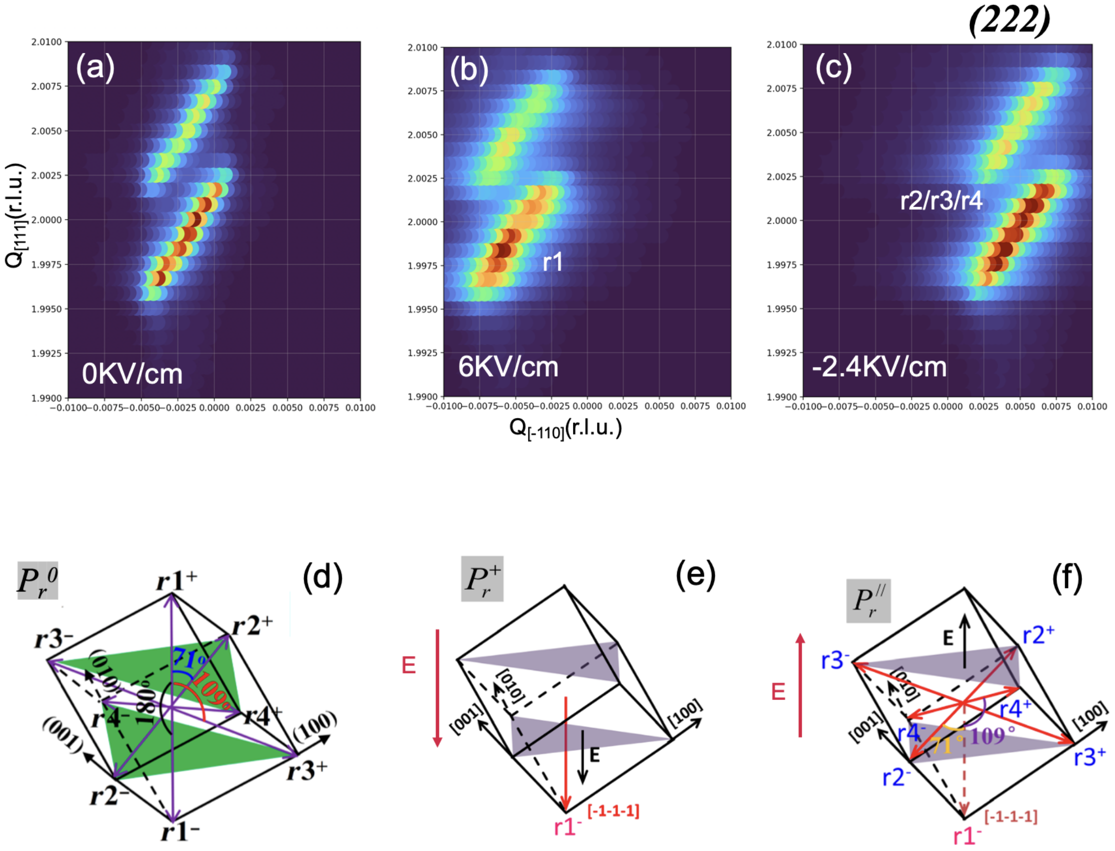

Figure 4.5: Reciprocal lattice map and Schematics of domain structures under different electric field about (222) reflections of PMN-PT(111). (a),(d) is for unpoled state. (b),(e) is under positive electric field with the downwards arrow in (e). (c),(f) is applying the coercive field of -2.4kV/cm. Electric field induced ferroelectric polarization switching is clearly demonstrated in the RSM

To confirm the specific domain switching pathways the RSMs are plotted also in the vicinity of the (-112) reflection. Due to the change of reflection plane, r1, r2 and r3/r4 can be distinguished by the different spot distributions clearly in the (-112) reflection in the initial state(Figure4.6(d)). On applying the positive voltage on the sample, r3/r4 polarization vanishes to align with the electric field along out-of-plane. The domain distribution of r1 and r2 can be quantitatively determined from the (-112) reflection shown in Figure4.6(b). After applying the negative coercive field, the r1 and r2 polarization undergoes a 71° and 109° domain switching to r3 and r4. Therefore, the stable and reversible ferroelectric/ferroelastic domain switching pathway is confirmed. Analysis of the peak intensities of different polarization variants is listed in the Table4.4 according to the method of Yang,et.al [43, 4]. Since the rotation from r1 to r3/r4 is 109° and r1 to r2 is 71°, the reduction of r1 corresponds to the 71° and 109° domain switching.

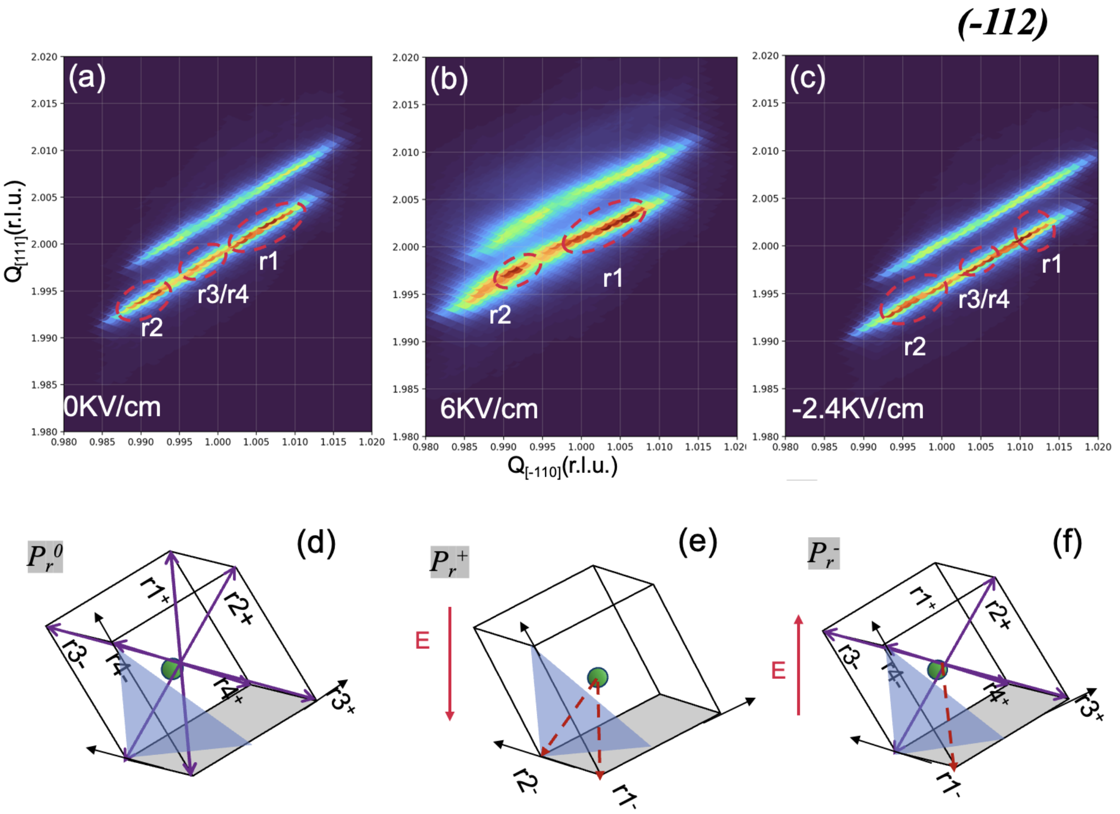

Figure 4.6: Reciprocal lattice map and Schematics of domain structures under different electric field about (-112) reflections of PMN-PT(111). (a),(d) is for unpoled state. (b),(e) is under positive electric field. (c),(f) is applying the coercive field of -2.4kV/cm. Electric field induced ferroelectric polarization switching is clearly demonstrated in the RSM

Table 4.4: Percentages of different polarization variants under positive and negative electric fields for sample LSMO/PMN-PT(111)

Voltage	r1	r2	r3/r4
0kV/cm	$42.1\%^{+0.01}_{-0.02}$	$26.3\%^{+0.02}_{-0.03}$	$31.6\%^{+0.02}_{-0.03}$
+6kV/cm	$73.4\%^{+0.01}_{-0.02}$	$16.6\%^{+0.01}_{-0.02}$	
-2.4kV/cm	$20\%^{+0.02}_{-0.02}$	$46.7\%^{+0.02}_{-0.02}$	$33.3\%^{+0.02}_{-0.03}$

In PMN-PT(001), through the analysis of positions and intensities of the spots (in support materials) according to the method of Yang, et.al [43, 4], the percentages of different polarization variants under positive and negative electric fields are listed in Table4.5. The results suggest that the proportion of r2/r4 under -4kV/cm is about 23% less than that under +4kV/cm. Since the change between r2/r4 and r1/r3 corresponds to the 109°, the reduction of r2/r4 proportion indicates that most part of the net proportion of switching is 109°. The comparison points out the advantage of poling a (111)-oriented PMN-PT over a (001)-oriented PMN-PT where only the 109° domain switching facilitates the in-plane lattice strain.

Table 4.5: Percentages of different polarization variants under positive and negative electric fields for sample LSMO/PMN-PT(001)

Voltage	r1/r3	r2/r4
+4kV/cm	$54.3\%^{+0.03}_{-0.05}$	$45.7\%^{+0.02}_{-0.03}$
-4kV/cm	$64.9\%^{+0.01}_{-0.02}$	$35.1\%^{+0.04}_{-0.02}$

4.4 Magnetic characterisation of LSMO thin film

For the sample LSMO/PMN-PT(111) the temperature dependent magnetisation measurement with the magnetic field along the [-110] direction reveals that the Curie temperature of LSMO is about 305K in zero-field cooling(ZFC) and field cooling curves(FCC) under the 50mT magnetic field(Figure4.7(a)), while for LSMO/PMN-PT(001) the Curie temperature is about 315K(Figure4.7(b)) which is closer to the bulk crystal. Lower Curie temperature is related to strained epitaxy thin film. But due to the manufacturing error, the composition of LSMO thin film is changed from 30% Sr to 20% Sr, which also leads to the lower Curie temperature of the thin film. It should be investigated more in the next work.

Since the Curie temperature of Mn_3O_4 is 43K, the kink in the magnetization at around 43K presents the existence of Mn_3O_4 [9]. The Mn_3O_4 particles forms at the interlayer due to their chemical compatibility with the whole manganite perovskite family denoted by Tanvi Bhatnagar-Schöffmann et.al [6].

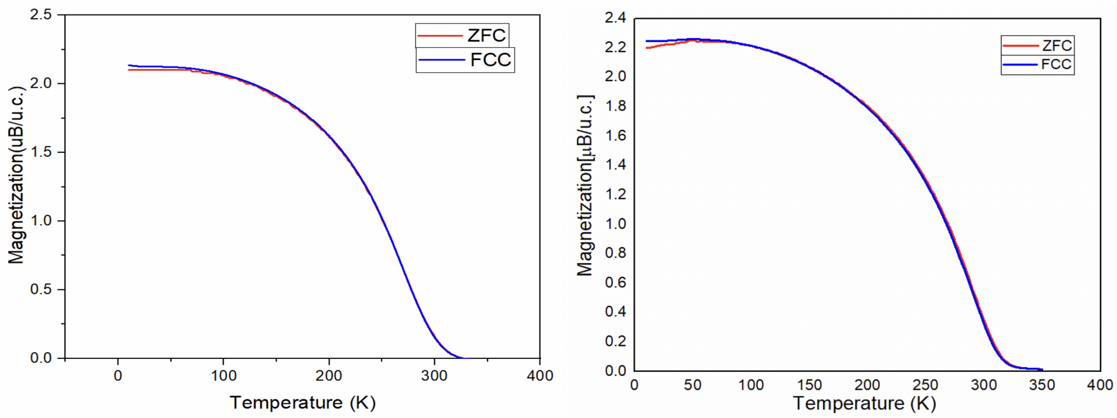

(a) ZFC/FCC curve of sample LSMO/PMN-PT(111) (b) ZFC/FCC curve of sample LSMO/PMN-PT(001)

Figure 4.7: (a) is the ZFC and FCC curve of LSMO/PMN-PT(111) with T_c=305K .(b) is the the ZFC and FCC curve of LSMO/PMN-PT(001) with T_c=315K

The magnetization as a function of applied magnetic field at different temperature is depicted in Fig4.8 showing a stable ferromagnetic state of LSMO. But on PMN-PT(111) substrate the hysteresis and coercive field is samller than PMN-PT(001), which indicates the influence of large mismatch in (111) direction and the quality of LSMO thin film is not so good as (001).

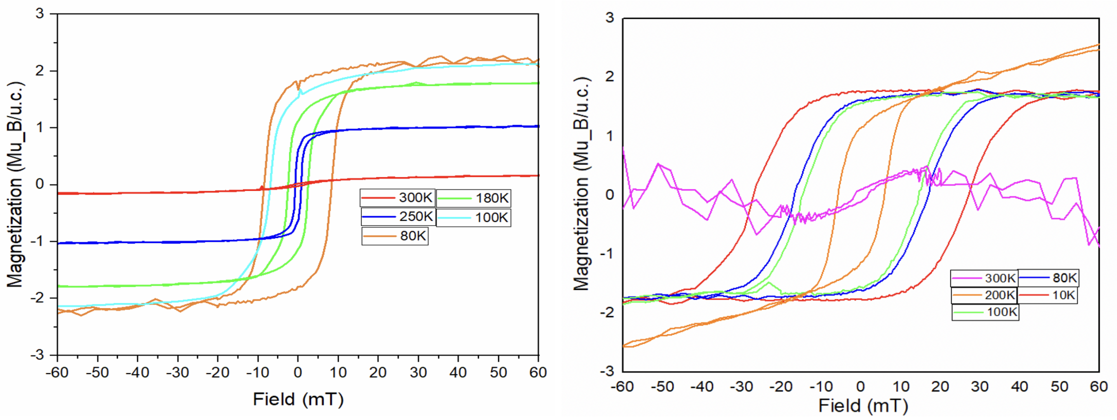

(a) Hysteresis curve of sample LSMO/PMN-PT(111) (b) Hysteresis curve of sample LSMO/PMN-PT(001)

Figure 4.8: Hysteresis curve of sample LSMO/PMN-PT(111) and (001)

4.5 Magnetoelectric coupling of LSMO/PMN-PT heterostructure

After confirming the magnetic and structural properties, the effect of substrate strain and electric polarisation on the magnetisation of the magnetic layer is probed. Magnetoelectric coupling measurements were performed with SQUID. The sample was coated with a gold layer and adopted the Ag-paste in contact with the outside electric field. The electric field is applied along the out-of-plane direction, i.e. [111] and [001], and magnetic field is in [-110],[11-2] direction for PMN-PT(111), in [100] for PMN-PT(001). The ME behaviour is investigated as a function of temperature with the magnetic field. The measurements are recorded at two temperatures 300K and 50K and 50mT magnetic fields since the magnetization in LSMO/PMN-PT is near saturation, but not saturated [5]. Therefore, the influence of both magnetic and electric field can be observed.

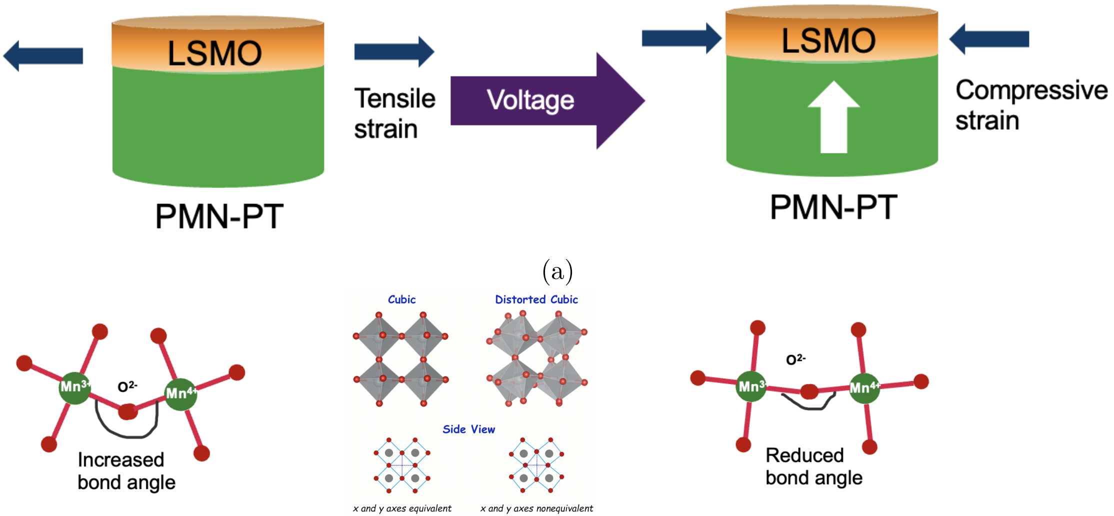

(a)

(b) (c) (d)

Figure 4.9: Schematic of the mechanism of strain-mediation in LSMO/PMN-PT.(b) and (c) explain the distortions of MnO_6 octahedra cause an decrease in bond angle and decrease in hopping matrix element.(d) With the increase in bond angle , electron hopping enhances giving rise to ferromagnetic ordering.

Due to the lattice mismatch between LSMO and PMN-PT, the LSMO thin film experiences a high in-plane tensile strain which results in the distortions of MnO_6 octahedra. The element of increased Mn-O-Mn bond angle disables the electron hopping in double exchange interaction according to Hubbard model the hopping probability t depends on the bond angle Θ via $t = t_0 cos(\pi - \theta)^2$. Therefore, the distorted structure destabilizes the ferromagnetism. When applying the voltage in the sample, the PMN-PT substrate experiences in-plane compressive strain due to the polarisation aligning with the electric field and transfers to LSMO, weakening the lattice mismatch. As a result, the distortion of MnO_6 relieves and the Mn-O-Mn bond angle tends to return to its original state towards 180°, which is easy for electron hopping. Therefore, the ferromagnetism is optimised. The strain mediation is depicted in Figure4.9.

Figure 4.10 shows the ME coupling observed at 300K on LSMO/PMN-PT(111) and LSMO/PMN-PT(001). The electric field loops follow 0kV/cm to +4kV/cm to 0kV/cm to -4kV/cm to 0kV/cm, similar to the polarization measurement. The magnetic moments of LSMO follow both the magnetic and electric fields. The asymmetrical butterfly loop with the cross-over point around +1kV/cm and +0.4kV/cm respectively indicates that there are other effects contributing to it besides strain-mediated coupling. The ME coupling curve shows different shapes under different directions of magnetic field, which is related to magnetic anisotropy. The hard axis of LSMO is [001] and easy axis is [110]. The difference in magnetization at 300K between negative and positive is about 0.02% (111) and 0.6% (001).

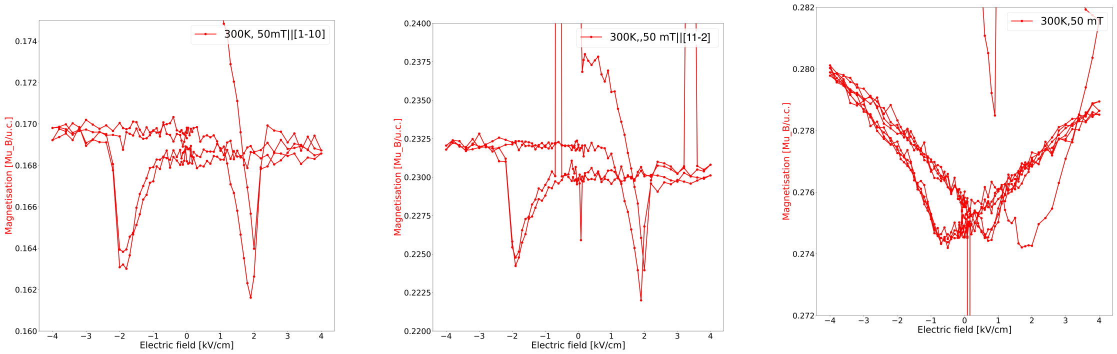

(a) 300K, 50mT parallel to [1-10] direction

(b) 300K, 50mT parallel to [11-2] direction

(c) 300K, 50mT parallel to [110] direction for PMN-PT(001

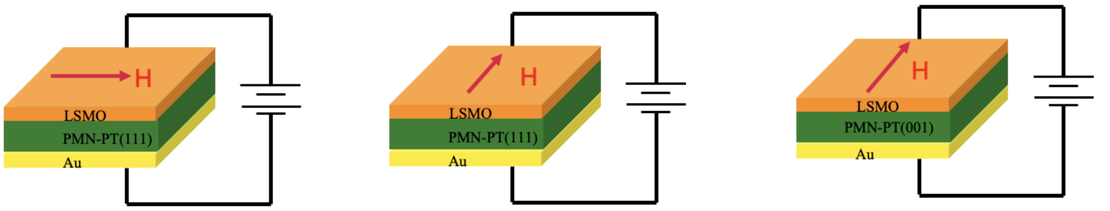

Figure 4.10: Magnetization as a function of electric field at 300K and the schematic of the measurement under different magnetic field direction.

The presence of ferroelectricity also makes charge mediated coupling plausible. For sample LSMO/PMN-PT(111), when applying the negative voltage, the polarization in PMN-PT substrate rotates towards [111] direction, resulting in the negative charge accumulation of LSMO at interface as presented in Fig4.11(b). The accumulation of negative charges reduces the Mn^{4+} ions and further strengthens the double exchange interaction. This is responsible for enhanced magnetization. Nonetheless, the accumulation of positive charges reduces the magnetisation under positive voltage. Therefore, a higher magnetization is obtained for -V and lower magnetization for +V as shown in Fig4.10.

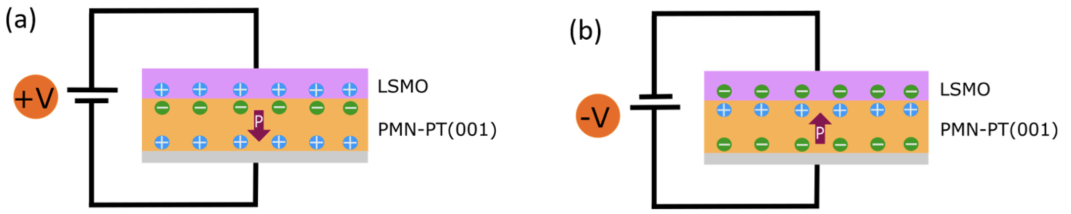

(a) (b)

Figure 4.11: (a)Schematics of the interface charge distribution with applied positive voltage.(b)applied negative voltage in the LSMO/PMN-PT(001) heterostructure. Draw adapted from [6].

The second measurement is performed at 80K with 50mT , presenting a different ME behaviour compared to the one at 300K . The piezoelectric strains are significantly reduced at low temperature resulting in hardening rotation of polarization [42]. Also, the electric coercive field is very high and the FE polarization cannot be switched with this small amount of electric field as shown in the research of Jinhwan Kim et.al (Figure4.12) [24]. For the measurement at 80K, the sample is already poled with negative bias voltage from the last voltage cycle and in strained state. When -4kV/cm is applied along out-of-plane direction, the polarization pointing upwards tends to align with the electric field (Fig.4.13 left) and leads to compressive strain, contributing to the enhancement of the magnetization. Under +4kV/cm, the polarization tends to rotate following the positive electric field direction. However it can't fully rotate resulting in the tensile strain as shown in Figure4.13(a). The change in strain is very small for PMN-PT(111) because for PMN-PT(111), the polarization variant r1 is along the [111] direction the same with the electric field direction as shown in Figure4.13(a) left. The strain induced by rotation(Figure4.13(a) right) is not so obvious therefore the difference of the magnetization is also very small as shown in Figure 4.14. The ME coupling at 80K is strain-mediated dominant. The systematic error is about 4.2% for the absolute value of the magnetization caused by the area and thickness of thin film.

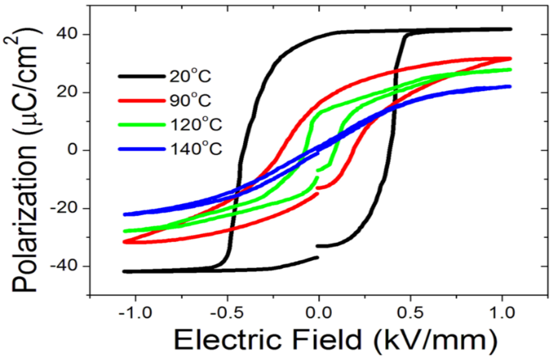

Figure 4.12: Ferroelectric polarization hysteresis at different temperature of PMN-PT taken from [24].

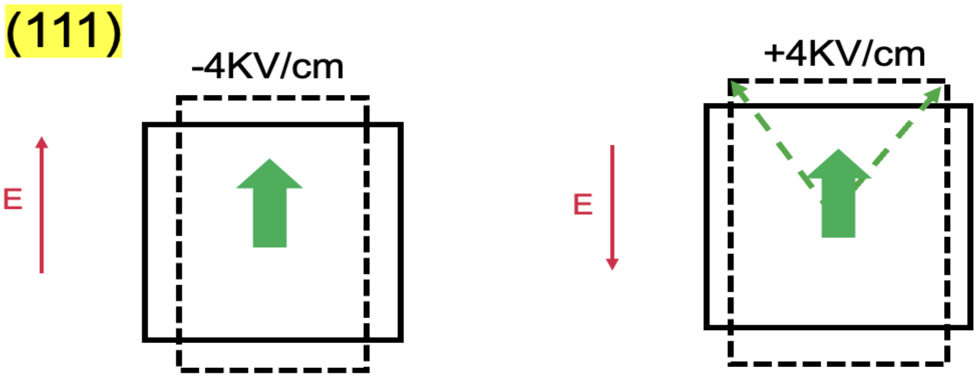

(a) Strain mediation in LSMO/PMN-PT(111) at 80K

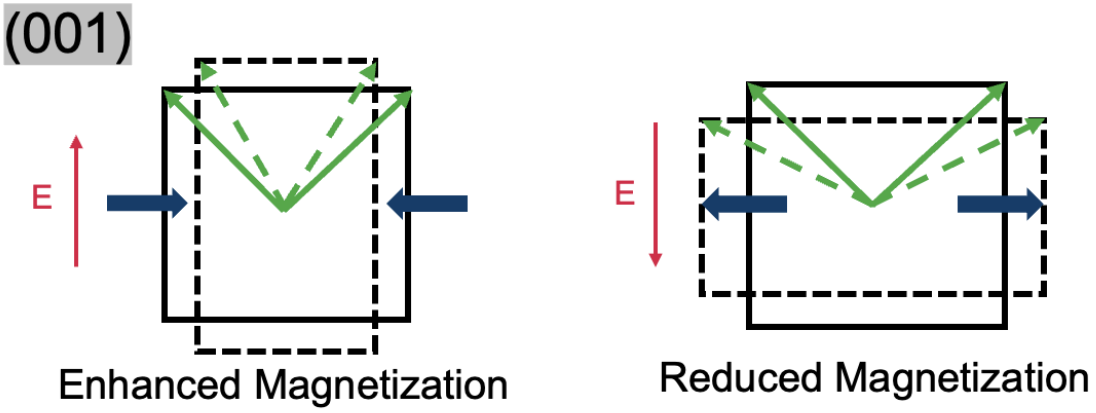

(b) Strain mediation in LSMO/PMN-PT(001) at 80K inspired from [6]

Figure 4.13: Schematic representing the strain-mediation taking place at 80K under positive and negative electric field for LSMO/PMN-PT(111) and (001). The dashed arrows depict the shift of ferroelectric polarizations in PMN-PT.

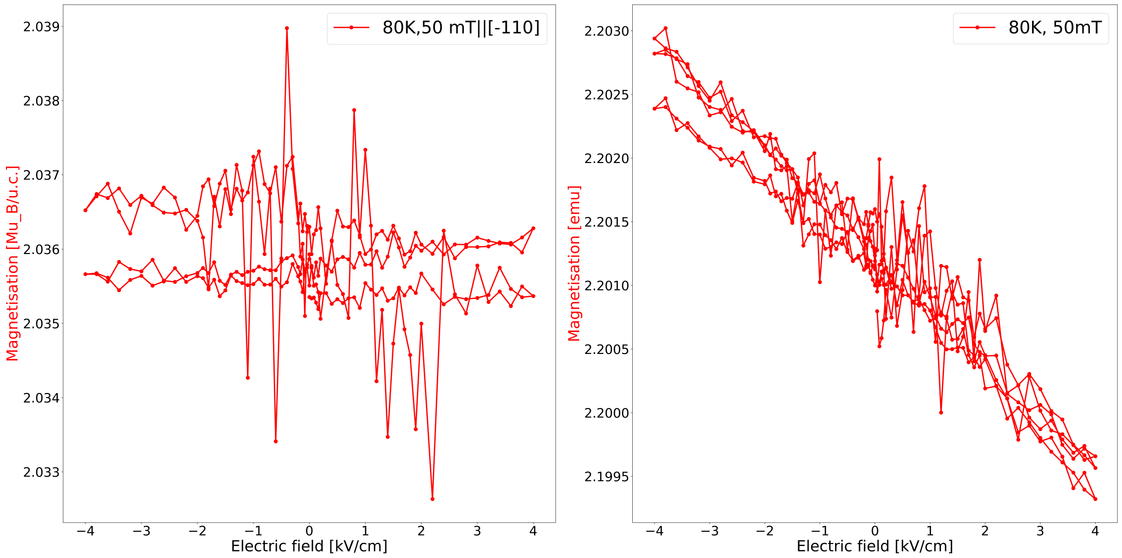

(a) ME curve of LSMO/PMN-PT(111) at 80K under 50mT magnetic field

(b) ME curve of LSMO/PMN-PT(001) at 80K under 50mT magnetic field

Figure 4.14: Magnetization as a function of electric field cycled at 80K for LSMO/PMN-PT(111) and (001)

4.6 Magnetoelectric coupling correlation with the domain switching

Application of an external electric field reorganizes the FE domain structure via domain-switching process, thereby modulating the magnetization via the strain effect with loop-like and butterfly-like M-E behaviour according to the research of Li et.al [25] and schematically in Figure4.15. For PMN-PT(111), the projections of polarizations to the (111) plane before and after 71/109° switching induces in-plane compressive strain, whereas after 180° switching the strain is along out-of-plane direction as shown in Figure4.16. For the 71/109° domain switching, the rhombic distortion changes from in-plane to the out-of-plane axis thereby changing the strain. In this case, the magnetic anisotropy and consequently the in-plane magnetization of the LSMO thin film can be controlled by electric fields resulting in the loop-like ME behaviour. For the 180° domain switching, domain switching produces a change of strain with a butterfly-like strain versus electric field curve. Therefore, the electric field control of the magnetization shows the butterfly-like ME behavior.

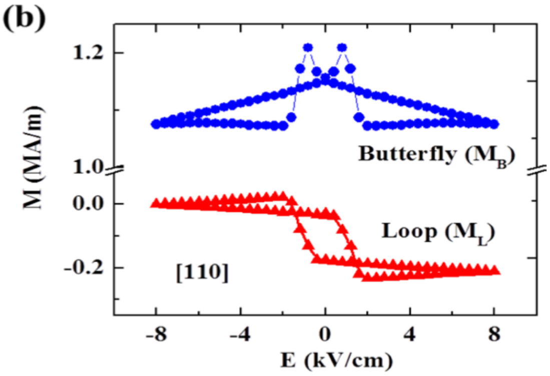

Figure 4.15: The loop-like(ML,red line) and butterfly-like(MB, blue line) electric-field control magnetization ME curves reprinted from [25]

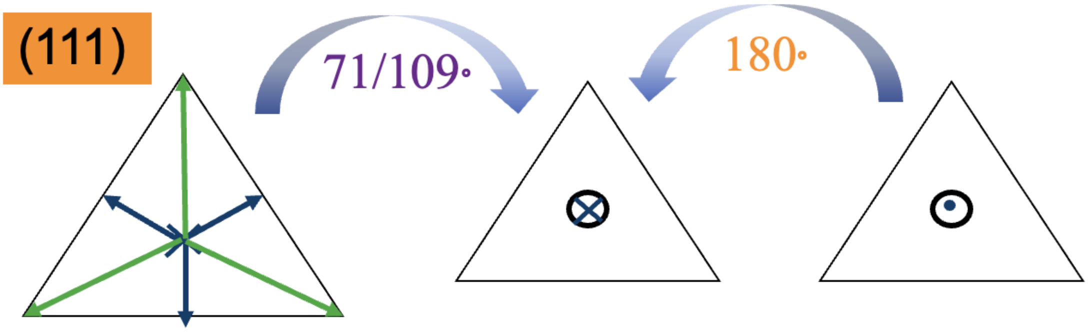

Figure 4.16: Projections of polarizations to the (111) plane before and after 71/109° switching and 180° and corresponding changes of distortion

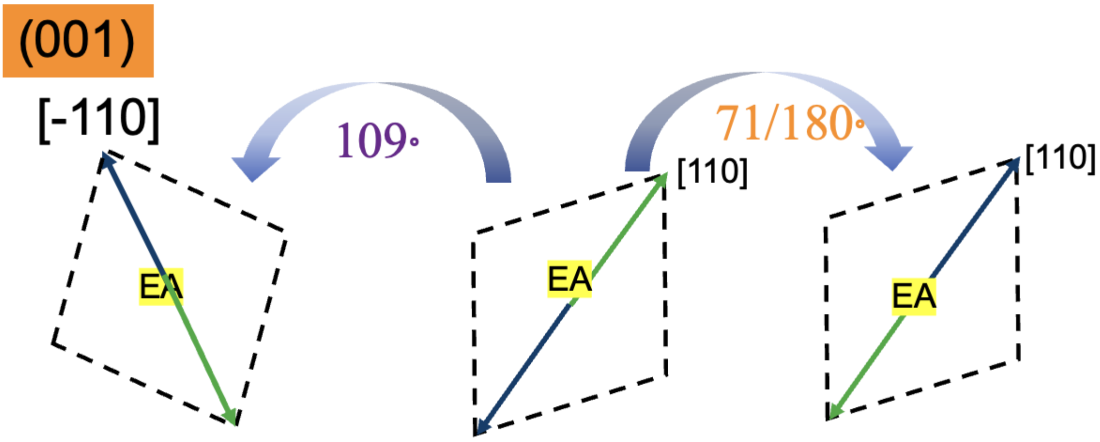

Figure 4.17: Projections of polarizations to the (001) plane before and after 109° switching are perpendicular

While for PMN-PT(001), the projection of polarizations to (001) plane before and after 109° switching is perpendicular, but after 71/180° is parallel. In this case, the elongated diagonal of rhombic distortion changes from [110] axis to [-110] axis thereby the strain state is altered after 109° switching. The electric field control of magnetization is loop-like behavior. For the 71/180° in PMN-PT(001), the direction of elongated diagonal does not change so the ME curve is similar to the butterfly-loop.

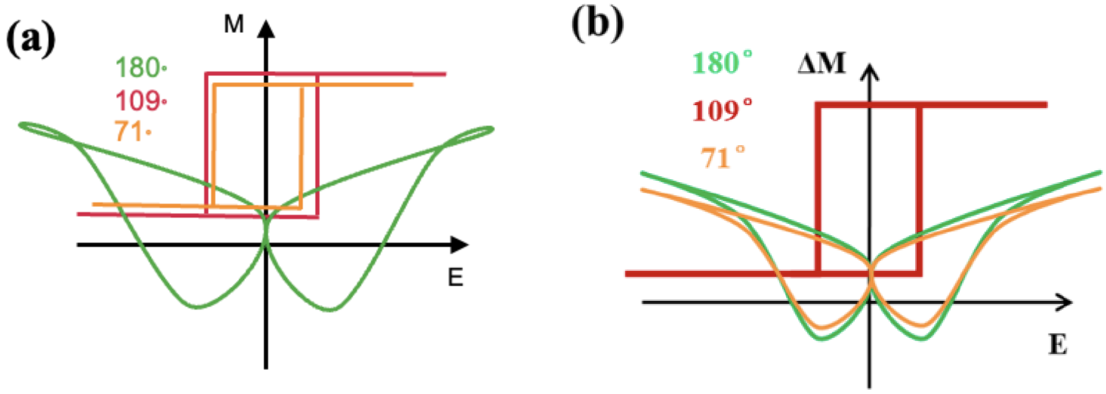

(a)

(b)

Figure 4.18: Picture of the simulated ME curves for LSMO/PMN-PT(111) and LSMO/PMN-PT(001) related to different domain switching inspired from [25]

The loop-like behavior is related to the non-volatile magnetization since after removing the electric field the magnetization is still remaining. By de-coupling the two different shapes of domain switching, the ME curves can be simulated. The ratio of different domain switching in a system is sample specific. For PMN-PT(111), 71/109° domain switching has a large contribution while for PMN-PT(001), 71/180° domain switching is dominant. Therefore, PMN-PT(111) has a better performance of non-volatile magnetization.

By removing the voltage, the polarizations don't switch back to their initial state due to ferroelectric effect and hard rotation of 109° domain switching. Besides, the accumulation of positive and negative charges at the LSMO/PMN-PT interface continues to change the magnetization. Therefore, the non-volatile strain part and ferroelectric effect jointly contribute to the remanent change in magnetization. The charge mediation influenced ME curve is also the loop-like as seen in Figure4.19 from the research of [6]

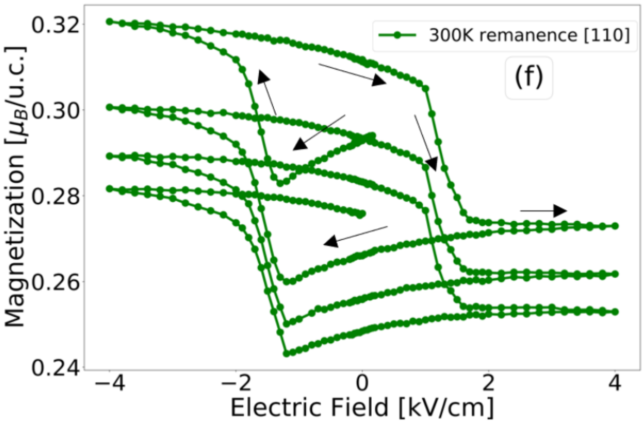

Figure 4.19: ME curve measured with remanent magnetic field along [110].Taken from [6]

Chapter 5

Conclusion

In this thesis, artificial multiferroic heterostructures, where the magnetization can be manipulated by electric field, was investigated. The sample was collected from the PMN-PT substrate with the LSMO thin film grown on it and back coated with the gold layer. Different planes of PMN-PT (001) and (111) were compared. This thesis aims to apply the electric and magnetic fields on the sample to find the relationship between the domain structure and correlation with magnetoelectric properties.

The reciprocal lattice measurement demonstrates that the domain switching with regarding to the polarization changes with the electric field. Through comparing the different reflections in LSMO/PMN-PT(111) under different voltage, variations of domain structure are clearly identified in the RSMs. Unlike in the (001) plane where the 109° switching dominates, the 71° and 109° degree switching in the (111) plane plays the big role jointly in domain switching.

In the magnetoelectric coupling measurement, the change of ME curves from butterfly to linear as a function of temperature due to the polarisation influenced strain-coupling. The temperature influence is different in (111) and (001) plane with regarding to the different polarization states. At 300K, the asymmetrical butterfly loop revealed the charge-coupling related to the ferroelectric properties of PMN-PT substrate, which presented higher magnetization under negative electric field and lower magnetization under positive electric field. Also the magnetic anisotropies decide the different butterfly shapes of ME curves for PMN-PT(111) and (001) plane.

Through analysis the relationship between domain switching and shape of ME curve, 71/109° domain switching has a large contribution and is dominant for the non-volatile magnetization for (111) plane and 109° domain switching is dominant for the non-volatile magnetization for (001) plane. Besides, the remanent magnetization is also correlated with the non-volatile strain part and ferroelectric effect in charge-mediation. These results provided a comprehensive understanding of magnetoelectric coupling in LSMO/PMN-PT with the investigation of crystalline structure under different electric field.

During the course of this thesis work, the same composition, thickness and experiment parameter of $La_{0.7}Sr_{0.3}MnO_3$ is controlled deposited on PMN-PT (111) and (001) plane. And all the analysis and results are based on this condition. But due to the manufacturing error, the composition of LSMO thin film is changed from 30% Sr to 20% Sr, which may have an effect on the lattice constant, Curie temperature and magnetic performance of the sample. It should be investigated more in the next work.

Appendix A

Supporting Material for Chapter 4

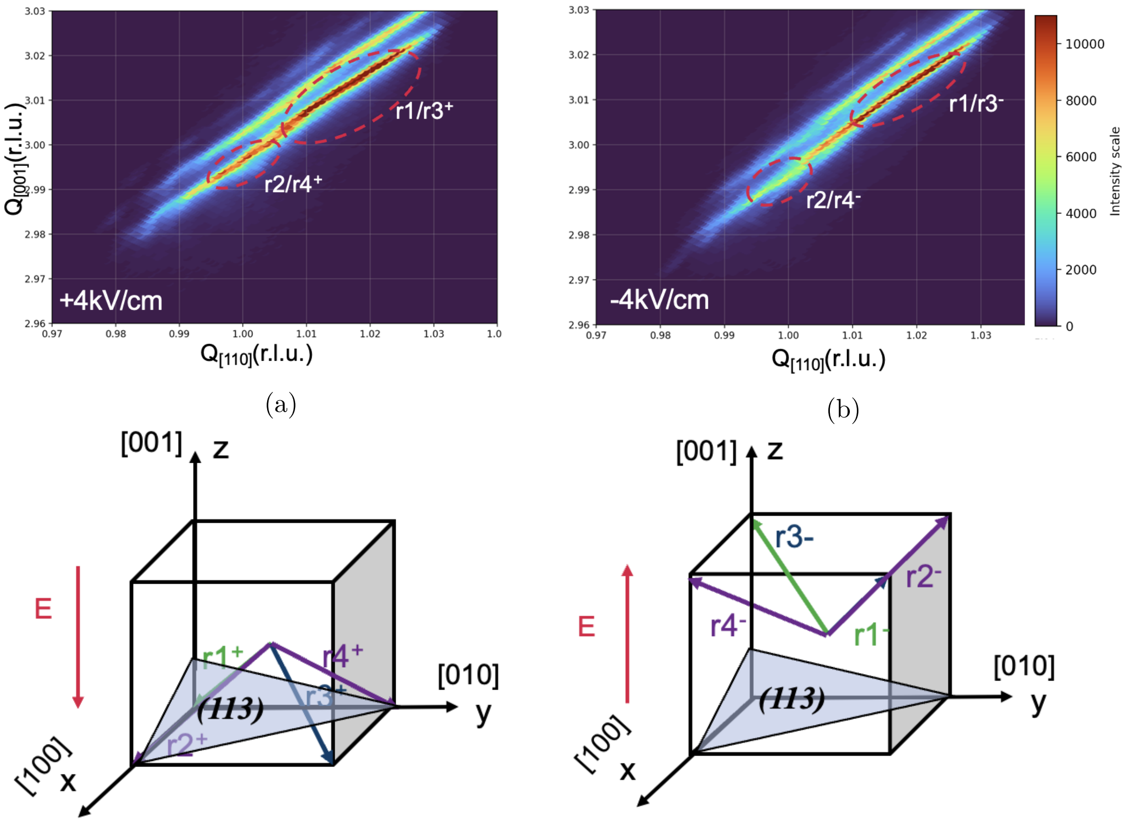

(a) (b)

(c) (d)

Figure A.1: (a) and (b) are Zoomed reciprocal lattice map in normal scale under positive and negative electric field.Ellipses with different colors in RSMs outline the contours of the deduced spots.(c) and (d) are Configurations of the (113) crystal face and polarisation variants of rhombohedral phase under positive and negative electric fields.

Bibliography

[1] Magnetic property measurement system: Mpms xl, hardware reference manual.

[2] `https://icsd.fiz-karlsruhe.de/index.xhtml;jsessionid=9E435C47B33278762608064156CF42AA`.

[3] Quantum design. magnetic property measurement system: Reciprocating sample option user's manual. 2001.

[4] S. Baek, H. Jang, C. Folkman, Y. Li, B. Winchester, J. Zhang, Q. He, Y. Chu, C. Nelson, M. Rzchowski, et al. Ferroelastic switching for nanoscale non-volatile magnetoelectric devices. *Nature materials*, 9(4):309–314, 2010.

[5] T. Bhatnagar. *Resolving interface effects in voltage controlled magnetic heterostructures using advanced neutron scattering and electron microscopy methods.* Dissertation, RWTH Aachen University, Jülich, 2021. URL `https://juser.fz-juelich.de/record/893740`. Dissertation, RWTH Aachen University, 2021.

[6] T. Bhatnagar-Schöffmann, E. Kentzinger, A. Sarkar, P. Schöffmann, Q. Lan, L. Jin, A. Kovacs, A. Grutter, B. Kirby, R. Beerwerth, et al. Differentiation between strain and charge mediated magnetoelectric coupling in $La_{0.7}Sr_{0.3}MnO_3/0.7Pb(Mg1/3Nb2/3) - 0.3PbTi_{0.3}O_3(001)$. *New Journal of Physics*, 2021.

[7] P. Borisov, A. Hochstrat, X. Chen, W. Kleemann, and C. Binek. Magnetoelectric switching of exchange bias. *Physical review letters*, 94(11):117203, 2005.

[8] P. Borisov, A. Hochstrat, V. Shvartsman, and W. Kleemann. Superconducting quantum interference device setup for magnetoelectric measurements. *Review of Scientific Instruments*, 78(10):106105, 2007.

[9] B. Boucher, R. Buhl, and M. Perrin. Magnetic structure of Mn_3O_4 by neutron diffraction. *Journal of Applied Physics*, 42(4):1615–1617, 1971.

[10] T. Brückel, G. Heger, D. Richter, R. Zorn, and G. Roth. *Laboratory Course Neutron Scattering: Lectures.* Forschungszentrum Jülich GmbH, 2011.

[11] M. Buzzi. *Spin dynamics in ferroic materials.* PhD thesis, University_of_Basel, 2015.

[12] A. Ceccucci. Acta physica polonica b editorial office: Review and outlook on kaon physics. *Acta Phys. Pol. B*, 49:1079–1086, 2018.

[13] C.-G. Duan, J. P. Velev, R. F. Sabirianov, W.-N. Mei, S. S. Jaswal, and E. Y. Tsymbal. Tailoring magnetic anisotropy at the ferromagnetic/ferroelectric interface. *Applied Physics Letters*, 92(12):122905, 2008.

[14] M. Eremenko, V. Krayzman, A. Bosak, H. Playford, K. Chapman, J. Woicik, B. Ravel, and I. Levin. Local atomic order and hierarchical polar nanoregions in a classical relaxor ferroelectric. *Nature communications*, 10(1):1–9, 2019.

[15] M. I. Faley. *High oxygen pressure deposition and patterning methods for metal oxide heterostructures.* Forschungszentrum Jülich GmbH, 2017.

[16] H. Fang. *Novel Devices Based on Relaxor Ferroelectric PMN-PT Single Crystals.* Springer Nature, 2020.

[17] Z. Feng, D. Lin, H. Luo, S. Li, and D. Fang. Effect of uniaxial stress on the electromechanical response of¡ 001¿-oriented $Pb(Mg1/3Nb2/3)-0.7PbTi_{0.3}O_3$. *Journal of applied physics*, 97(2):024103, 2005.

[18] L. Gerhard, T. Yamada, T. Balashov, A. Takács, R. Wesselink, M. Däne, M. Fechner, S. Ostanin, A. Ernst, I. Mertig, et al. Magnetoelectric coupling at metal surfaces. *Nature Nanotechnology*, 5(11):792–797, 2010.

[19] A. Glavic. *Multiferroicity in oxide thin films and heterostructures*, volume 45. Forschungszentrum Jülich, 2012.

[20] A. Haghiri-Gosnet and J. Renard. Cmr manganites: physics, thin films and devices. *Journal of Physics D: Applied Physics*, 36(8):R127, 2003.

[21] J. Ho, K. Liu, and I. Lin. Study of ferroelectricity in the PMN-PT system near the morphotropic phase boundary. *Journal of materials science*, 28(16):4497–4502, 1993.

[22] E. Kentzinger. *Laboratory Course Neutron Scattering - Neutron Reflectometry,.* Forschungszentrum Jülich GmbH, 2017.

[23] E. Kentzinger, M. Krutyeva, and U. Rücker. GALAXI: Gallium anode low-angle x-ray instrument. *Journal of large-scale research facilities JLSRF*, 2:61, 2016.

[24] J. Kim, S. Yoon, J.-H. Ji, Y.-H. Ko, K.-H. Cho, S.-K. Lee, and J.-H. Koh. Enhanced ferroelectric and piezoelectric properties of (1- x)PMN-xPT ceramics based on a partial oxalate process. *Materials*, 11(11):2247, 2018.

[25] P. Li, Y. Zhao, S. Zhang, A. Chen, D. Li, J. Ma, Y. Liu, D. T. Pierce, J. Unguris, H.-G. Piao, et al. Spatially resolved ferroelectric domain-switching-controlled magnetism in $Co_{40}Fe_{20}B_{20}/Pb(Mg1/3Nb2/3)-0.7PbTi_{0.3}O_3$ multiferroic heterostructure. *ACS applied materials & interfaces*, 9(3):2642–2649, 2017.

[26] M. Liu, O. Obi, Z. Cai, J. Lou, G. Yang, K. S. Ziemer, and N. X. Sun. Electrical tuning of magnetism in Fe_3O_4/PZN–PT multiferroic heterostructures derived by reactive magnetron sputtering. *Journal of Applied Physics*, 107(7):073916, 2010.

[27] P. Mangin and R. Kahn. *Superconductivity: an introduction.* Springer, 2016.

[28] M. McElfresh. *Fundamentals of Magnetism and Magnetic Measurements featuring Quantum Design's Magnetic Property Measurement System.* 1994.

[29] R. Meyer, R. Waser, K. Prume, T. Schmitz, and S. Tiedke. Dynamic leakage current compensation in ferroelectric thin-film capacitor structures. *Applied Physics Letters*, 86(14):142907, 2005.

[30] H. J. Molegraaf, J. Hoffman, C. A. Vaz, S. Gariglio, D. Van Der Marel, C. H. Ahn, and J.-M. Triscone. Magnetoelectric effects in complex oxides with competing ground states. *Advanced Materials*, 21(34):3470–3474, 2009.

[31] T. Schenk, E. Yurchuk, S. Mueller, U. Schroeder, S. Starschich, U. Böttger, and T. Mikolajick. About the deformation of ferroelectric hystereses. *Applied physics reviews*, 1(4):041103, 2014.

[32] M. Schmelz and R. Stolz. Superconducting quantum interference device (SQUID) magnetometers. In *High Sensitivity Magnetometers*, pages 279–311. Springer, 2017.

[33] M. Schmitz, A. Weber, O. Petracic, M. Waschk, P. Zakalek, S. Mattauch, A. Koutsioubas, and T. Brückel. Strain and electric field control of magnetism in $La_{(1--x)}Sr_xMnO_3$ thin films on ferroelectric $BaTiO_3$ substrates. *New journal of physics*, 22(5):053018, 2020.

[34] P. Schöffmann. *Stoichiometric control and magnetoelectric coupling in artificial multiferroic heterostructures.* Dissertation, RWTH Aachen University, Jülich, 2021. Dissertation, RWTH Aachen University, 2021.

[35] A. H. SIHVOLA and I. V. Lindell. Material effects in bi-anisotropic electromagnetics. *IEICE transactions on electronics*, 78(10):1383–1390, 1995.

[36] C. Song, B. Cui, F. Li, X. Zhou, and F. Pan. Recent progress in voltage control of magnetism: Materials, mechanisms, and performance. *Progress in Materials Science*, 87:33–82, 2017.

[37] G. L. Squires. *Introduction to the theory of thermal neutron scattering.* Cambridge University Press, 1978.

[38] C. Thiele, K. Dörr, O. Bilani, J. Rödel, and L. Schultz. Influence of strain on the magnetization and magnetoelectric effect in $La_{0.7}A_{0.3}MnO_3$/ PMN- PT (001)(A= Sr, Ca). *Physical Review B*, 75(5):054408, 2007.

[39] E. Y. Tsymbal, E. R. Dagotto, C.-B. Eom, and R. Ramesh. *Multifunctional oxide heterostructures.* Oxford University Press, 2012.

[40] K. Uchino. Relaxor ferroelectric-based ceramics. In *Advanced Piezoelectric Materials*, pages 127–153. Elsevier, 2017.

[41] C. Vaz, J. Hoffman, Y. Segal, J. Reiner, R. Grober, Z. Zhang, C. Ahn, and F. Walker. Origin of the magnetoelectric coupling effect in $(001)Pb(Zr_{0.2}Ti_{0.8})O_3/La_{0.8}Sr_{0.2}MnO_3$ multiferroic heterostructures. *Physical Review Letters*, 104(12):127202, 2010.

[42] L.-M. Wang, O. Petracic, S. Mattauch, A. Koutsioumbas, X.-K. Wei, M. Heggen, V. Leffler, S. Ehlert, and T. Brückel. Magnetoelectric coupling in iron oxide nanoparticle—barium titanate composites. *Journal of Physics D: Applied Physics*, 52(6):065301, 2018.

[43] L. Yang, Y. Zhao, S. Zhang, P. Li, Y. Gao, Y. Yang, H. Huang, P. Miao, Y. Liu, A. Chen, et al. Bipolar loop-like non-volatile strain in the (001)-oriented $0.7Pb(Mg1/3Nb2/3) - 0.3PbTi_{0.3}O_3$ single crystals. *Scientific reports*, 4(1):1–5, 2014.

[44] Z.-G. Ye, Y. Bing, J. Gao, A. Bokov, P. Stephens, B. Noheda, and G. Shirane. Development of ferroelectric order in relaxor $(1-x)Pb(Mg1/3Nb2/3)-xPbTi_{0.3}O_3$. *arXiv preprint cond-mat/0208058*, 2002.

[45] L.-L. Zhang and Y.-N. Huang. Theory of relaxor-ferroelectricity. *Scientific reports*, 10(1):1–18, 2020.

[46] S. Zhang and F. Li. High performance ferroelectric relaxor-pbtio3 single crystals: Status and perspective. *Journal of Applied Physics*, 111(3):2, 2012.

[47] S. Zhang, N. P. Sherlock, R. J. Meyer Jr, and T. R. Shrout. Crystallographic dependence of loss in domain engineered relaxor-PT single crystals. *Applied physics letters*, 94(16):162906, 2009.

[48] S. Zhang, Y. Zhao, P. Li, J. Yang, S. Rizwan, J. Zhang, J. Seidel, T. Qu, Y. Yang, Z. Luo, et al. Electric-field control of nonvolatile magnetization in $Co_{40}Fe_{20}B_{20}/Pb(Mg1/3Nb2/3) - 0.7PbTi_{0.3}O_3$ structure at room temperature. *Physical Review Letters*, 108(13):137203, 2012.

[49] W. Zhou, Q. Li, Y. Xiong, Q. Zhang, D. Wang, Q. Cao, L. Lv, and Y. Du. Electric field manipulation of magnetic and transport properties in $SrRuO_3/Pb(Mg_{1/3}Nb_2/3)O_3 - PbTiO_3$ heterostructure. *Scientific reports*, 4(1): 1–5, 2014.

List of Figures

List of Tables

Acknowledgements

I sincerely thank all of them for helping me in different ways to finish this thesis.Without the support of lots of people this thesis is not possible to be finished.

Prof.Dr.Thomas Brückel for providing me the opportunity to work at JCNS-2 on such an interesting research topics and for the support and suggestions for my work and thesis reviewing.

Prof.Dr.Joachim Mayer for supervisor and support for my work and thesis reviewing.

Dr.Emmanuel Kentzinger for the great guidance and support during my experiment, my research direction and thesis reviewing. Working in the GALAXI together and learning from his expertise was invaluable developing my own skills.He is very patient and professional to answer my questions and help me to solve the problem.

Dr.Tanvi Bhatnagar-Schöffmann and **Dr. Patrick Schöffmann** for the fruitful support and guidance to my reaserch. Working on the SQUID together I learned a lot experiment skills and data analysis from them. Thanks for the discussions and help to solve many problems

Jianwei Ye, Zhiyu Pan and Zhipeng Bao for their help in teaching me Python to analyze the WAXS data. Without their patient and professional explain and emotional support I can't finish this thesis.

Jan Lübben for the great guidance and support in Polarisation-Electric field measurement in IWE-2 RWTH.

Prof.Dr.Renkui Zheng for supporting my experiment in sending me the new substrates.

Chenyang Yin,Yifan Xu and Mengying Tang for for various experimental training and measurements.

Dr. Ulrich Rücker for help and support in the X-ray lab of JCNS-2.

Jansen Thomas for help in substrate coating in PGI-6.

Dr. Oleg Petracic for help and support at MPMS.

Dr. Connie Bednarski-Meinke, **Dr.Mai Hussein** and **Dr.Asmaa Qdemat** for discussions and supports.

Berthold Schmitz and **Frank Gossen** for technical supports on HOPSD and MPMS

Finally, I would like to express my thanks to all the members at JCNS-2 for the friendly atmosphere. Last but not least, I am very grateful to my parents and friends for their unfailing love and tolerating.